INVESTIGATION OF TAYLOR IMPACT TEST OF ISOTROPIC AND ANISOTROPIC MATERIAL THROUGH GEOMETRICAL CHARACTERSTICS OF SPECIMENS

by

ZHIYI CAO

A THESIS

Submitted in partial fulfillment of the requirements
for the degree of Master of Science in the
Department of Aerospace Engineering and Mechanics
in the Graduate School of
The University of Alabama

TUSCALOOSA, ALABAMA

2010

ABSTRACT

In this thesis, high strain rate properties of isotropic material (a copper alloy) and anisotropic material (2195-T8 aluminum-lithium alloy) are investigated using Taylor impact tests. Coordinate measuring machines (CMMs) are used to measure the shape of specimens after the deformation. The geometrical data enables us to determine the plastic distributions and the dynamic yield stresses of specimens. A raise in yield strength is found in the copper alloy during the impact. It means that material properties of the copper alloy are sensitive to high strain rate. Yet such phenomenon is not found in the 2195-T8 aluminum-lithium alloy. Based on the uniaxial compression strain state in the barreling regions of the specimens, the dynamic yield stresses in the rolling, transverse and short transverse directions are obtained for the 2195-T8 aluminum-lithium alloy. This enables us to determine the anisotropic coefficients in Hill's criterion and carry out the finite element analysis. The dependencies of fracture are also investigated. It is found that the fracture is sensitive to maximum shear stress, equivalent plastic strain and stress triaxiality.

DEDICATION

To my parents and grandpa

LIST OF SYMBOLS

Latin Symbols

A_0, A_f =cross-sectional area of the specimen before and after the deformation

A, B, C, n, m = material constants in the Johnson-Cook model

c_p =specific heat

e =compressive strain

F, G, H, L, M, N =coefficients of anisotropic plasticity in Hill's criterion

h =distance from the impact surface to the plastic wave front

h_0, h_f =length of the segment before and after the deformation

h_a, h_b = axial location of points *a* and *b* on an un-deformed specimen

$\Delta h, \Delta H$ =the distance between points on an un-deformed and deformed specimen, respectively

H_A, H_B = axial location of points A and B on a deformed specimen

l =length of the un-deformed region

$\bar{l}$ = length that the plastic wave produced during the initial transient cannot cover in the specimen

l_f = length that the plastic wave with a constant strain e cannot cover in the specimen

L_0 =original length of the specimen

L_b =length of the barreling region

L_f =final overall length of the deformed specimen

r_0 , r_a , r_b =original radius of the specimen, radii of the major and minor sides after the deformation

$\overline{R}$ = radius of the equivalent cylinder

R_{11} , R_{22} , R_{33} , R_{12} , R_{13} , R_{23} =coefficients of anisotropic plasticity

R_A , R_B = radius at the A and B measuring point respectively

s =displacement of the back end of the specimen

$\bar{s}$, s_f = displacements of the back end of the specimen at the end of the impact and at the end of the initial transient

T = temperature of specimens during the Taylor impact tests

T^* = homologous temperature

T_0 = reference temperature

T_m = melt temperature

u = velocity of the material at the plastic wave front

v =velocity of the un-deformed section

v_0 =impact velocity

Greek Symbols

α =fraction of the plastic work converted to heat

β =dimensionless constant relation material velocities before and after the plastic wave front

ε_p = equivalent plastic strain

$\dot{\varepsilon}_p$ = plastic strain rate

$\dot{\varepsilon}_{p0}$ = reference plastic strain rate

$\dot{\varepsilon}_p^*$ = dimensionless plastic strain rate

ε_a^p, ε_b^p =plastic strain in the major and minor radial directions

ε_{rr}^p = plastic strain in the radial direction

$\varepsilon_{\theta\theta}^p$ = plastic strain in the θ direction

ε_{zz}^p = plastic strain in the axial direction

λ =proportionality factor

ρ =material density

σ =dynamic yield stress

σ_0 =reference stress

σ_r, σ_t, σ_{st} =dynamic yield stresses in the rolling, transverse and short transverse directions

σ_s =quasi-static yield stress

σ_y = flow stress

ACKNOWLEDGMENTS

It is with a deep sense of gratitude that I acknowledge the excellence guidance, patience and support of my advisor Dr. Mark E. Barkey throughout my studies and the period of this thesis. Also, I would like to express my sincere thanks and appreciation to my committee members, Dr. Stan E. Jones and Dr. Yuebin Guo for their valuable comments and suggestions.

I gratefully acknowledge Eric Weishaupt and Dave Metz for the microhardness test and helpful discussions on the material microstructure. Dr. Jones assistants, Jennifer Conway and Tony Oritz are also thanked for the help on the Taylor impact test.

I wish to thank my parents for their support in my career. Finally, I wish to thank all my friends for being there and making my stay in Tuscaloosa a very memorable one.

CONTENTS

LIST OF TABLES

LIST OF FIGURES

CHAPTER 1

INTRODUCTION

1.1 Motivation and Objectives

The strength of materials under high strain rate has been a subject for formal study for more than two centuries. Current interest in this subject is due largely to the concerns of the safety of vehicles during a crash, the penetration of projectiles and high-strain-rate machining. Many methods were proposed to investigate the strength of materials under high strain rate, such as Split Hopkinson Pressure Bar test (SHPB), flyer plate impact test and Taylor impact test. However, the strain rates that are possible in the Split Hopkinson Pressure Bar are limited by the elastic wave speed in the bars. On the other hand, flyer plate tests are very expensive to conduct and instrument, and they produce ultra high strain rates in the order of 10^6-$10^8 s^{-1}$. The Taylor impact test was proposed by G. I. Taylor in 1940s [1]. It consists of a normal impact of a flat-ended cylindrical projectile onto a rigid massive target, and can be used to determine the dynamic compressive strength of a material. The typical strain rate in this test can achieve 10^3-$10^6 s^{-1}$.

The objective of this thesis is to investigate the plastic strain distribution and the dynamic yield stresses under varying levels of strain and strain rate (for anisotropic material also in different directions) through the shapes of specimens after impact. Coordinate measuring machines (CMMs) are used to determine the plastic strain

distribution of the specimens, which enable us to determine the dynamic yield stresses. The materials investigated are a copper alloy and 2195-T8 aluminum-lithium alloy. Finite element simulation is performed to validate the strain distribution and the dynamic yield stresses. The dependencies of the fracture are also discussed.

1.2 Thesis Organization

This thesis starts with an introductory chapter (Chapter 1). A brief background on impact tests, especially Taylor impact test, is described. The objective and motivation of this research is stated.

Chapter 2 reviews the research work involving Taylor impact test and the accuracy of CMMs.

Chapter 3 presents the experimental procedures and material properties. Procedures of Taylor impact test and post test measurements are described. The materials investigated in this thesis are a copper alloy and 2195-T8 aluminum-lithium alloy. Results of quasi-tension tests and microhardness tests of these materials are presented.

Chapter 4 is the core of the dissertation. In this chapter, the plastic strain distributions of the specimens (a copper alloy) are determined through FEM analysis and CMM calculation. The results show that the stress state in the barreling zone is uniaxial compression. Based on this, we expand our investigation to anisotropic material, the 2195-T8 aluminum-lithium alloy. Its dynamic yield stresses in the rolling, transverse, and short transverse directions are obtained. The evolution of its

anisotropy under large strain and high strain rate is investigated. The FEM analysis is carried out to validate the analysis. The shapes of the specimens produced by FEM are compared with those produced by experiments. The dependencies of fracture are discussed.

Based on the results presented in previous chapters, Chapter 5 gives conclusions of this thesis, and suggestions for future work.

CHAPTER 2

LITERATURE REVIEW

2.1 Taylor Impact Test

2.1.1 Introduction and Advances in Taylor Impact Test

The Taylor impact test consists of a normal impact of a flat-ended cylindrical projectile onto a rigid massive target. Figure 2.1 is a copper alloy specimen before and after the impact. During the impact, compressive stress waves are generated at the impact surface and traverse in the projectile. If the impact velocity of the projectile is sufficiently high, both elastic wave and plastic wave will be generated. Due to the higher tangent modulus of a material in the elastic zone, the speed of elastic wave is faster than that of plastic wave. Therefore the compressive waves will have two components. The leading component is elastic wave which traverses at the speed of sound in the material. The plastic wave follows the elastic wave at a much slower speed. The compressive elastic wave reflects on the end and returns as tensile elastic wave. The interaction of the plastic wave and the reflected elastic wave progressively dissolute the energy that plastic wave carries, and stop the propagation of the plastic wave.

The Taylor impact test was originally used to estimate the dynamic yield strength of ductile metals. Taylor [1] reported that the dynamic yield strength was a function of the changes in dimension of the specimen. According to his theory, the flow stress of

the material can be determined through the length of the un-deformed section at the back end of the specimen. In Taylor's analysis, material particles are assumed to come to rest completely after they pass across the plastic wave front. The approximation produces a useful estimate for dynamic yield stress, which tends to be somewhat high. This analysis was modified and improved by several investigators. In particular, Jones et al. [2-4] gave a one-dimensional analysis that subtracted the initial transient, dominated by the shock at impact, from the subsequent quasi-steady deformation. With improved techniques for accurately measuring very small specimens, the analysis has been applied to a wide variety of metals, e.g. Russo, et al. [5].

Recently the Taylor impact test is more often applied to determine the strain-rate dependent material coefficients and demonstrate the quality of a numerical code in computational plastic mechanics. Brünig et al. [6] used the explicit finite element program LS-DYNA augmented by a user-defined material subroutine to simulate the behavior of stainless steel in the Taylor impact test. Banerjee [7] presented a comprehensive report on numerical modeling of the Taylor impact test. He compared the deformed profile of specimens with numerical results at varying impact speeds, temperatures and plasticity models. A wide range of strain and strain rates (quasi static to $8000\,s^{-1}$) were examined in the tests. With varied temperatures (room temperature to more than $1000\,K$) of specimen, the relation between dynamic yield stress and temperature was investigated. In his work, five plasticity models--Johnson-Cook, Steinberg-Cochran-Guinan-Lund, Zerilli-Armstrong, Mechanical Threshold Stress, and Preston-Tonks-Wallace--produced deformed shapes close to those experimentally

observed at room temperature. However, large differences between the deformed shape of the numerical simulations and the experimental profiles occurred at high temperatures.

2.1.2 Taylor's Analysis

To construct the model, Taylor ignores the radial inertia and assumes that the problem is one dimensional. He also assumes the rigid-plastic model of stress-strain relationship. Figure 2.2 shows the nomenclature defined in Taylor's analysis. The original length of the specimen is L_0. The length that is traversed by the plastic wave is h. The length that is unaffected by the plastic wave is l. The displacement of the rear end of the specimen is s. Connecting the length of the specimen before and after the impact, we have

$$L_0 = h + l + s . \tag{2-1}$$

Differentiating the equation with respect to t, time, we get

$$0 = \dot{h} + \dot{l} + \dot{s} . \tag{2-2}$$

Since h is the displacement of the plastic wave relative to the impact surface, $\dot{h}$ is the Eulerian plastic wave speed. $\dot{s} = v$ is the velocity of the rear end of the specimen. Taylor assumes that all the material unaffected by the plastic wave shares the same velocity $\dot{s}$, and gets

$$\rho l \frac{d^2 s}{dt^2} = -\sigma_y , \tag{2-3}$$

where ρ and σ_y are the mass density and dynamic yield stress respectively. Taylor continues his analysis with the conservation of mass

$$\rho A_f dh = \rho A_0 dx, \tag{2-4}$$

where A_0 and A_f are the cross-sectional area of the specimen before and after the impact. Dividing both side by ρdt, Equation (2-4) becomes

$$A_f \dot{h} = A_0 \dot{x}. \tag{2-5}$$

Eliminating $\dot{x}$ (noticing that $\dot{x} = -\dot{l}$), Equation (2-2) and Equation (2-5) reduce to

$$A_f \dot{h} = A_0(\dot{S} + \dot{h}). \tag{2-6}$$

Taylor assumes that material comes to rest instantaneously as it crosses the plastic wave front, which is not exactly correct [8]. This assumption leads to a strain discontinuity at the elastic-plastic interface. Consider an element at the edge of elastic-plastic interface at time t, and this element crosses the interface at time $t + dt$. The momentum equation of this element is

$$\rho A_f \dot{s}\, dl = \sigma_y (A_f - A_0) dt. \tag{2-7}$$

Now consider Equation (2-3) again,

$$\frac{d\dot{s}}{dt} = \frac{d\dot{s}}{dl}\frac{dl}{dt} = -\frac{\sigma_y}{\rho l}. \tag{2-8}$$

Substituting Equation (2-2) into Equation (2-8) gives

$$\frac{d\dot{s}}{dl} = \frac{\sigma_y}{\rho l(\dot{s} + \dot{h})}. \tag{2-9}$$

Separating and integrating the variables, Taylor gives

$$\int_{v_0}^{0} (\dot{s} + \dot{h}) d\dot{s} = \int_{l_0}^{l_f} \frac{\sigma_y}{\rho l} dl, \tag{2-10}$$

where v_0 is the impact velocity. l_0 is the initial un-deformed length, which is also the length of the specimen before the impact, l_f is the final un-deformed length. To eliminate the plastic wave speed $\dot{h}$, Taylor assumes that $\dot{h}$ is a constant during the

wave propagation. The assumption of constant plastic wave speed gives

$$t_f = \frac{L_f - l_f}{\dot{h}}, \tag{2-11}$$

where t_f is the duration of the impact event, and L_f is the final total length of the specimen after the impact. Taylor assumes that the deceleration of the specimen during the impact is constant:

$$t_f = \frac{2(L_0 - L_f)}{v_0}. \tag{2-12}$$

Eliminating t_f between Equation (2-11) and (2-12), the plastic wave speed is

$$\dot{h} = \frac{v_0(L_f - l_f)}{2(L_0 - l_f)}. \tag{2-13}$$

Substituting Equation (2-13) into Equation (2-10) gives the expression for the dynamic yield stress:

$$\sigma_y = \frac{\rho v_0^2 (L_0 - l_f)}{2(L_0 - L_f)(\ln L_0 - \ln l_f)} \tag{2-14}$$

The method proposed by Taylor is approximated. Material particles cannot stop immediately after crossing the plastic wave front [8]. The plastic wave speed is not constant due to strain hardening. The validation of constant deceleration of the specimen during the impact is also doubtful. Although Taylor calculates that the global strain rate is approximately $10^4 s^{-1}$ in the test, the strain rate varies with time and position throughout the specimen.

2.1.3 Jones's anaysis

Due to the deficiencies in Taylor's analysis, S. E. Jones proposed some modifications based on the physical phenomena of impact.

As shown in Figure 2.3, consider an element at the interface of elastic-plastic wave at time t. This element will be fully deformed at time $t+\Delta t$ due to the plastic wave. The axial strain in the element is constant as long as the length of the element is small. Since no voids grow during the deformation, the conservation of the mass can be expressed in the form of the conservation of volume. The conservation of the mass during the elapse Δt gives:

$$-uA_0\Delta t + vA_0\Delta t = A_f\Delta l - A_0\Delta l\,, \tag{2-15}$$

where u is the particle velocity of the plastic material behind the plastic wave ($u=0$ in Taylor's analysis), and v is the velocity of the un-deformed section. Dividing Equation (2-15) by $\Delta t A_i$ and taking the limit as $\Delta t \to 0$, it gives

$$-u + v = \frac{A_f}{A_0}\dot{x} - \dot{x}\,. \tag{2-16}$$

Since the dynamic stress calculated is along the axial direction, we need to relate $\frac{A_f}{A_0}$ to $\frac{h_f}{h_0}$. Using the conservation of volume,

$$\pi r_0^2 h_0 = \pi r_f^2 h_f \tag{2-17}$$

and

$$\frac{\pi r_f^2}{\pi r_0^2} = \frac{A_f}{A_0} = \frac{h_0}{h_f}\,. \tag{2-18}$$

Defining

$$\frac{h_0 - h_f}{h_0} = e \tag{2-19}$$

and eliminating $\frac{A_f}{A_0}$, Equation (2-16)-(2-19) reduce to

$$e\dot{l} = v - u, \tag{2-20}$$

where v and u are the particle velocity before and after the plastic wave respectively, and l is the length of the un-deformed zone. As discussed in [8], the relation between the particle velocity behind and before the plastic wave front after the initial transient is:

$$u = \beta v. \tag{2-21}$$

Substitute Equation (2-21) into Equation (2-20) gives

$$(1-\beta)v = e\dot{l}. \tag{2-22}$$

By separating the variables, we have

$$dl = (\frac{1-\beta}{e})ds. \tag{2-23}$$

Equation (2-21) only holds true after the attenuation of the initial transient at impact. A certain plastic wave associating with a constant strain e moves away from the impact surface. Therefore, we integrate Equation (2-23) along the distance traveled by the certain plastic wave with a constant strain e after the initial transient, and get:

$$l_f - \bar{l} = \frac{1-\beta}{e}(s_f - \bar{s}). \tag{2-24}$$

l_f is the length that the plastic wave with a constant strain e cannot cover in the specimen. $\bar{l}$ is the length that plastic wave cannot cover in the specimen during the initial transient. s_f and $\bar{s}$ are the displacements of the back end of the specimen at the end of the impact and at the end of the initial transient impact. Dividing Equation (2-24) with L_0, we express the equation in the following form:

$$\frac{l_f}{L_0} = -\frac{1-\beta}{e}\frac{L_f}{L_0} + \frac{\bar{l}}{L_0} + \frac{1-\beta}{e} - \frac{1-\beta}{e}\frac{\bar{s}}{L_0}. \tag{2-25}$$

Equation (2-25) describes a linear relationship between l_f/L_0 and L_f/L_0. Using the data from the coordinate measuring machine, we can determine the positions of the specimen cross-sections with the same e among the different specimens. β can then be determined according to the slope of the line that best fits the data..

To estimate the stress, the momentum equation of the shaded element is required:

$$\rho A_0 \Delta l v - \rho A_0 \Delta l u = \frac{\sigma A + (\sigma + \Delta\sigma)(A + \Delta A) - \sigma_0 A_0 - (\sigma_0 + \Delta\sigma_0)A_0}{2}\Delta t. \tag{2-26}$$

Dividing by Δt and taking the limit as $\Delta t \to 0$, Equation (2-26) gives

$$\rho A_0 l (v - u) = \sigma A - \sigma_0 A_0. \tag{2-27}$$

Substitute Equation (2-22) into Equation (2-27), we get:

$$\rho \dot{l} v (1-\beta) = \frac{\sigma}{1+e} - \sigma_0, \tag{2-28}$$

where σ is the compressive dynamic yield stress during the quasi-steady motion, and σ_0 is the reference stress. In order to match quasi-static yield stress as $v \to 0$, we define

$$\sigma_0 = \sigma_s/(1+e), \tag{2-29}$$

where σ_s is the quasi-static yield stress. For a certain level of compressive strain e, we can determine the corresponding β according to the final reversed shapes of the Taylor specimens.

Taylor's analysis is improved by introducing the dimensionless coefficient β to relate the particle velocity before and after the plastic wave. However, this analysis also contradicts Taylor's analysis by taking the stress on the elastic side of the elastic-plastic interface as quasi yield stress (σ_0 in Equation (2-28)). In Taylor's

analysis, the stress before the plastic wave front is regarded as dynamic yield stress (Y in Equation (2-7)). Considering the existence of the elastic wave before the elastic-plastic interface, taking the stress as dynamic stress is more reasonable.

2.2 Coordinate Measuring Machine

To determine the dynamic yield stress, the geometrical data of specimens after impact is required. In this thesis, a coordinate measuring machine is used.

Coordinate Measuring Machines (CMMs) are mechanical systems designed to drive a measuring probe to determine the geometrical characteristics on the surface of a specimen or a component. CMMs consist of four main parts: the main structure that includes three axes of motion, the measuring probe, the control system, and the measuring software. According to the performance of measurement, there are two types of CMMs: optical and contacting. The comparison of the accuracy of these two types is given in [9]. It is believed that mechanical CMMs are as good as, if not better than, optical CMMs. The CMM used in thesis is mechanical type.

The reliability of CMMs is always an issue. Abbe et al. [10] and Paulo Cauchick-Miguel et al. [11] presented through discussions on the reliability and accuracy of CMMs. When selecting a CMM for an application, the total required measuring length and the mass of the work piece must be considered for making an appropriate measurement. Accuracy will decline if the total required measuring length or mass is beyond the CMM's capacity. Usually CMMs are used to obtain geometrical characteristics. In this thesis, we investigate the use of the CMM for experimental

determination of plastic strain distributions, using recovered Taylor impact test specimens as the work pieces.

The touch trigger probe of CMM may cause error. Cauchich Miguel et al. [11] investigated factors influencing CMM touch trigger probe performance. He reported several error sources such as the temperature during measuring tests, angles of approach of the probe, and stylus stem length. In our test, another factor influencing the probe accuracy is the radius of spherical probe tip of the CMM. The radius should be small enough so that the spherical tip will not be blocked by the narrow space at transition of mushroomed zone and barreling zone (Figure 2.4). Otherwise, accuracy will be comprised.

CHAPTER 3 EXPERIMENTAL PROCEDURES AND MATERIAL PROPERTIES

3.1 Experimental Procedures

3.1.1 Taylor Impact Test

During the Taylor impact test, a cylindrical specimen is launched from a smooth bored gun barrel to impact a rigid massive target normally. The target is made of a hardened steel face separated from a softer steel body by a thin copper plate. This is to assure that the deformation of the target is ignorable during the impact. The volume of the target is large enough to assure no effect due to a reflected elastic wave during the contact of the impact event. To minimize the effect of friction the target surface is polished to a mirror-like finished. The impact speeds were measured by the oscilloscope, and varied from $150\,m/s$ to around $300\,m/s$.

The copper alloy specimens were made of two different sizes: diameters $7\,mm$ and $12\,mm$. The length to diameter ratio is 7.5 for all, although small differences of the dimensions may occur in the machining of the specimens. Here we choose this ratio because a higher ratio may lead to dynamic buckling, while a lower ratio may lead to the absence of an elastic zone. Each specimen is machined $0.076\,mm$ under the bore diameter to permit an easy launch without jamming the gun tube. Figure 2.1 is a copper alloy specimen before and after the impact.

For the 2195-T8 aluminum-lithium alloy specimens, their diameters are all $5.4\,mm$ with the length-to-radius ratio 7.5. Each specimen is machined $0.076\,mm$ under the bore diameter to permit an easy launch without jamming the gun tube. The material is anisotropic. Specimens were cut parallel to the rolling direction. After impact, the originally cylindrical specimens with a circular cross-section have a deformed elliptical cross-section as shown in Figure 3.1. If the impact speed is high enough ($220\,m/s$ in Figure 3.1(c) (d) (g)), fracture happens near the impact surface region.

3.1.2 Metrology

A CMM is used to measure the copper and aluminum alloy specimens. Geometrical data of specimens after the impact were obtained by the 7.10.7 Global Performance Coordinate Measuring Machines equipped with a TESASTAR-SP25M probe at Brown & Sharpe, in Nashville, Tennessee. The spherical radius of the probe was $5\,mm$, and the length of the stem was $30\,mm$. The scanning speed is $10\,mm/s$, and during the measurement, the contacting force between the spherical tip and the specimen were in the range of $0.025\,N$ to $0.15\,N$. Measurements along the axial direction were made at regular intervals and processed using PC-DMIS software. The axial measurement intervals are approximately $2.5\,mm$, $0.1\,mm$ and $0.25\,mm$ for $7\,mm$-diameter copper specimens, $12\,mm$-diameter copper specimen and 2195-T8 aluminum-lithium alloy specimens respectively. The accuracy of the measurements was on the order of 1-2 μm. The measurement interval along hoop direction was 7.5

degree. Figure 3.2 shows the measurement in process.

3.1.3 Quasi-static tension test

Quasi-static tension tests are used to obtain quasi-static compressive strength for both the copper and aluminum alloy. Only yield stress (0.2% strain) is needed for the analysis of Taylor impact test. The difference of stress-strain curve between the tension and compression is ignorable at corresponding strain. Rectangular specimens are tested in a SATEC 20 *kip* capacity uniaxial testing machine. The MTS one-inch-gage-length extensometer is used to measure the engineering strain. The tests are conducted in displacement control, with an actuator displacement rate of $0.02\,inches/\min$.

3.2 Material properties

3.2.1 Copper Alloy

The copper we have is oxygen-free high conductivity (OFHC) under initial annealed condition.The OFHC copper has minimum a 99.95% copper. The data of quasi-static tension for OFHC copper is shown in Figure 3.3.

The crystal structure of copper is face-centered cubic (fcc). Materials with fcc structure generally exhibits a yield stress that is strain rate dependent. The Johnson-Cook model [12] is used to describe the stress-strain curve under high-strain rate:

$$\sigma_y(\varepsilon_p, \dot{\varepsilon}_p, T) = [A + B(\varepsilon_p)^n][1 + C\ln(\dot{\varepsilon}_p^*)][1 - (T^*)^m], \tag{3-1}$$

where σ_y is the flow stress, ε_p is the equivalent plastic strain, $\dot{\varepsilon}_p$ is the plastic strain rate, A, B, C, m, and n are material constants.

$$\dot{\varepsilon}_p^{\,*} = \frac{\dot{\varepsilon}_p}{\dot{\varepsilon}_{p0}} \quad , \tag{3-2}$$

$$T^* = \frac{T - T_0}{T_m - T_0} , \tag{3-3}$$

where $\dot{\varepsilon}_{p0}$ is a reference plastic strain rate, T_0 is a reference temperature, and T_m is the melt temperature. T_0 is selected as room temperature. Equation (3-1) is used in the FEM analysis. According to the ABAQUS Documentation, the parameters of Johnson-Cook model for an annealed OFHC copper are shown in Table 1.

Metallographic samples of the test specimens were sectioned and mounted for metallographic analysis. The samples were prepared following standard metallographic preparation procedures with a 0.05 micron colloidal silica wet abrading process functioning as a final polishing step. The un-deformed microstructure of the copper sample was initially characterized using a Nikon inverted metallograph, with the un-deformed microstructure presented in Figure 3.4. The transverse direction is depicted in Figure 3.4(a), while the longitudinal direction is presented in Figure 3.4(b). The observed microstructure is consistent with that of a low alloy copper. The microstructure displayed no distinguishable preferential direction due to cold working.

In addition to the microstructure characterization, microhardness measurements were conducted on the copper alloy samples with the results of these measurements presented in Table 2. Microhardness traverses were performed in the longitudinal

direction as well as in both the vertical and horizontal transverse direction. All measurements were performed using a Knoop indenter with a 50 gram load on a Tukon hardness tester. The microhardness results indicate that the copper displays a relatively uniform hardness in all directions (124 +/- 2 HK) in all directions.

It is apparent that the relatively fine grain size, lack of preferential direction imparted by cold working, and uniform hardness in the transverse and longitudinal directions, will produce a relatively isotropic material on the macroscopic scale, i.e., for the purposes of this study the bulk material is considered to be isotropic.

3.2.2 2195-T8 Aluminum-Lithium Alloy

The composition of the 2195-T8 aluminum-lithium alloy is as follows (wt %): 4.3Cu, 1.41Li, 0.03Si, 0.05Fe, 0.35Mg, 0.01Ni, 0.02Zn, 0.02Ti, 0.4Ag, 0.13Zr; balance Al.

Aluminum alloys are known to exhibit a low sensitivity to strain rate. Oosterkamp et al. [13] tested AA6082 and AA7108 and found that their strain rate sensitivity is very low. However, the strain rate in their tests is in the order of $10^3 s^{-1}$. In Taylor impact test, the strain rates can be as high as $10^4 - 10^6 s^{-1}$. Data of quasi-static tension tests is shown in Figure 3.5 and Figure 3.6. Tension specimens are cut parallel and perpendicular to the rolling direction respectively.

CHAPTER 4

RESULTS AND DISCUSSION

4.1 Copper Alloy Taylor Impact Test

4.1.1 Analytical Model of Strains

The basic steps involved to estimate plastic strain distributions in Taylor impact test specimens from the CMM measurements is to develop a model that maps a deformed specimen back to its original shape, and apply a suitable strain measurement. The geometry of the deformed Taylor impact specimens is well suited for this analysis. As in previous studies, the barreling region will be of primary interest, and it will be assumed that the stress state that existed in the barreling region was predominately uniaxial compression.

As a consequence of this assumption, originally plane cross-sections remain plane after the deformation. The deformed specimens are divided into segments according to the measurement intervals obtained from the CMM. Additionally, if the shear strains are also neglected, we can state that the strain state in one segment is constant as long as the axial measurement intervals are small. The shear strains in each segment can be effectively ignored in the areas of the specimen where the slope of the axial profile of the specimen is small. In the mushroom region where the slope is large, errors in the strain calculation may occur in the segments. However, in the barreling region where the slope is relatively small, the errors are also small.

Assuming that the profile that connects two measurement intervals is linear, we can divide the impacted specimen into many segments that take the shape of truncated cones, as in Figure 4.1(a). To further simplify the analysis, the truncated cones are transformed into an equivalent cylinder with equal volume and height, shown in Figure 4.1(b). The radius of the equivalent cylinder is:

$$\overline{R} = \frac{1}{\sqrt{3}}\left(R_B^2 + R_A R_B + R_A^2\right)^{1/2}, \tag{4-1}$$

for two consecutive radius measurement points along the axial direction, A and B, on the deformed specimen.

It is accepted that many metals satisfy the conservation of volume during plastic flow. Therefore, the truncated cone segment on the deformed specimen must have come from an un-deformed cylindrical segment of the un-deformed specimen with the same volume. Since the radius of the original cylinder and the volume of the truncated cone segment are known, the height of the un-deformed segment can be determined.

Due to the large amount of data obtained from the data of CMM measurement, the strains in the deformed cylinder can be determined in the following algorithmic manner:

Assume that points $a(r_o, h_a)$ and $b(r_o, h_b)$ on the surface of the un-deformed specimen transform to points $A(R_A, H_A)$ and $B(R_B, H_B)$ on the surface of the deformed specimen. The upper case symbols R and H reference the radius and longitudinal (axial) position of the points on the deformed specimen, and are determined for the points A and B by successive measurements from the CMM. The lower case symbols r_o and h reference the radius and longitudinal (axial) position of those points on the

un-deformed specimen. Since r_o is a known constant—the initial radius of the cylinder before testing—it is left to determine the original axial position of the points *a* and *b*.

The axial plastic strain can be determined by the distance between the points in the un-deformed and deformed specimens: i.e. $\Delta H = H_B - H_A$, $\Delta h = h_b - h_a$, and

$$\varepsilon_{zz}^{p} = \ln\left(\frac{\Delta H}{\Delta h} + 1\right). \tag{4-2}$$

The key element to determining the original distance between the points is to apply the conservation of volume of the cylindrical segment between the points in the un-deformed specimen and the volume of a truncated cone segment of an equivalent cylinder in the deformed specimen, $V_{ab} = V_{AB}$, which results in $\Delta h = \frac{\overline{R}\Delta H}{r_o}$. The location of the point *b* in the un-deformed cylinder can be established by

$$h_b = h_a + \Delta h, \tag{4-3}$$

and we have finished the transformation:

$$B(R_B, H_B) \rightarrow b(r_o, h_b).$$

In the barreling region, the stress state is primarly uniaxial compression in the cylindrical coordinate system. Therefore, no significant shear strains exist in this coordinate system. The strain state in a given segment is constant:

$$\varepsilon_{ij}^{p} = \begin{bmatrix} \varepsilon_{rr}^{p}, 0, 0 \\ 0, \varepsilon_{\theta\theta}^{p}, 0 \\ 0, 0, \quad \varepsilon_{zz}^{p} \end{bmatrix}, \tag{4-3}$$

where ε_{rr}^{p}, $\varepsilon_{\theta\theta}^{p}$, and ε_{zz}^{p} are plastic strains in the radial, hoop, and axial directions respectively. The conservation of volume in terms of strain is

$$\varepsilon_{rr}^{p} + \varepsilon_{\theta\theta}^{p} + \varepsilon_{zz}^{p} = 0, \tag{4-5}$$

and the assumption of isotropy gives

$$\varepsilon_{rr}^{p} = \varepsilon_{\theta\theta}^{p} \tag{4-6}$$

which when substituted into Equation (4-5), results in

$$\varepsilon_{rr}^{p} = -0.5\varepsilon_{zz}^{p}. \tag{4-7}$$

Therefore, all components in Equation (4-4) can be determined once ε_{zz}^{p} is fixed.

Other forms of strains can also be obtained since the coordinates of the points *a* and *b* and *A* and *B* are known.

4.1.2 Estimate of Dynamic Yield Stress

As we discussed in Chapter 2, the dynamic yield stress in the barreling zone is:

$$\sigma = (1+e)[\sigma_0 + \frac{(1-\beta)^2}{e}\rho v^2]. \tag{4-8}$$

β can be obtained from the deformed shape of specimens. σ_0 is a reference stress. In order to match quasi-static yield stress as $v \to 0$, we define

$$\sigma_0 = \sigma_s / (1+e), \tag{4-9}$$

where σ_s is the quasi-static yield stress. This estimate is only valid in Phase II, which is associated with formation of the barreling region. In this region, the dominating strain rate is around $2500\,s^{-1}$ to $4500\,s^{-1}$ when the impact speed is around $150\,m/s$ to $220\,m/s$. Recall the linear equation described the final deformed shape of the specimens:

$$\frac{l_f}{L_0} = -\frac{1-\beta}{e}\frac{L_f}{L_0} + \frac{\bar{l}}{L_0} + \frac{1-\beta}{e} - \frac{1-\beta}{e}\frac{\bar{s}}{L_0}. \tag{4-10}$$

It shows the linearity between l_f/L_0 and L_f/L_0. β can be determined from the slope of Equation (4-10). Table 3 is the values of β obtained through Figure 4.2. Selecting the quasi-static stress of the copper alloy, σ_s, as 280 MPa, dynamic yield stresses can be calculated. In Figure 4.3, the stresses compared are quasi-static data, Johnson-Cook model with strain rate 10000 s^{-1} and estimate of Equation (2-28). Figure 4.3 demonstrates that Equation (2-28) overestimates the dynamic yield stress, especially at small plastic strain level.

4.1.3 Finite element analysis of copper alloy specimens

The mesh of cylindrical specimen was produced in ABAQUS 6.9-1 and was refined with HYPERMESH 9.0. Triangular elements near the periphery of the specimen were produced during the refinement. With these triangular elements, the FEM simulation provided more axial symmetric deformation. An analytical rigid surface was applied to model the massive target. The cylindrical specimen impacted the rigid surface at the same speeds as those in the experiment. The calculations were performed for 90 μs, at which time the target and all plastic deformation had ceased.

Figure 4.4 shows a comparison between the logarithmic plastic radial strain calculated by the CMM and FEM based calculation methods. For the FEM calculation, the radial strain on the specimen surface was chosen for the comparison to the average strain calculated by the CMM method. Figure 4.4(a), (b) and (c) are for the 7 mm-diameter specimens, and Figure 4.4(d) and (e) are for the 12 mm-diameter specimens.

In the barreling region, the results of FEM and CMM methods for all specimens match quite closely. Comparing the results of the $7\,mm$-diameter specimens and $12\,mm$-diameter specimens, results of FEM and CMM-based calculation agree more closely for $7\,mm$-diameter specimens even though the measuring intervals were larger. This may due to the distribution of logarithmic plastic radial strain at a fixed axial position is more uniform in the $7\,mm$-diameter specimens.

Figure 4.5 shows the equivalent plastic strain distribution on the cross-section $14.8\,mm$ away from the impact surface (in the barreling region) for a $12\,mm$-diameter specimen. The figure indicates that the plastic strain distribution calculated by the finite element method at this position is uniform, indicating that the CMM-based calculation method is applicable in this region.

In the mushroom region, the FEM results and the CMM based calculation do not match. This is because the stress state in the mushroom region is a complex multiaxial stress state, which violates the uniaxial stress state assumption of our simplified analysis. In addition, the plot compares the surface strain calculated by the FEM method to the average strain calculated by the CMM-based method as described previously. However, even in the mushroom region, the CMM-based calculation gives reasonable behavior for the average plastic strain, since this strain increases with impact speed.

Comparing Figures 4.4(a) and (d), we can find that maximum strain determined by CMM-based calculation in mushroom region is smaller in $7\,mm$-diameter specimens than that in $12\,mm$-diameter specimens with equal impact speed. This

implies that the deformation in the mushroom region increases with mass. The same trend can be obtained when comparing Figures 3.1(b) and (e).

Figure 4.6 shows the equivalent plastic strain distribution at the impact surface calculated by the FEM method. It indicates that the plastic strains are higher at the center of the impact surface and are lower near the edge. This non-uniform plastic strain distribution is the source of the inconsistency between the results of the FEM and CMM-based calculations. The non-uniform plastic strain region extends further in the axial direction at a higher impact speed, since the mushroom region is longer. As a percentage of length, the mushroom region for the $12\,mm$-diameter specimens was shorter than in the $7\,mm$-diameter specimens at the same impact speed.

In general, the CMM-based calculation method for Taylor Impact Cylinder strains is applicable if the strain distribution is uniform in a segment, i.e. radially uniform for a fixed axial position. Different measuring intervals can be used to improve the measuring efficiency. Axial position of the segment, size of the specimen, and impact speed can influence the accuracy of the CMM-based calculation method.

4.2 2195-T8 Aluminum-Lithium Alloy Taylor Impact Test

4.2.1 Estimate of the Dynamic Yield Stress in the Axial Direction

Follow the same process, we can estimate the dynamic yield stress along the axial direction for 2195-T8 aluminum-lithium alloy. The equation to obtain the β value is given by Equation (4-10). Using the data from the CMM, we can determine the axial positions associated with a certain strain among different specimens. Fitting

the data with a linear equation β is determined. The relation between L_f/L_0 and l_f/L_0 of the 2195-T8 aluminum-lithium alloy specimens are shown in Figure 4.7. Values of β are determined from the slopes and shown in Table 4.

The dynamic yield stress is given by Equation (4-8). Combining Equation (4-8) with β from Table 4, the dynamic yield stresses can be obtained. In order the find out whether 2195-T8 aluminum-lithium alloy is sensitive to strain rate, a comparison between quasi-static data and estimates by Equation (4-8) is necessary. Figure 4.8 shows that the quasi-static data is close to the estimates except at 16% strain. The difference in 16% strain is due to its axial position, which is close to the mushroom region and nonlinear motion of the plastic wave front still affects this place. Therefore, it is reasonable to attribute the much-too-high stress at 16% strain to error, and state that 2195-T8 aluminum-lithium alloy is insensitive to strain rate. This conclusion is pivotal to the later analysis. Without shooting specimens cutting along the transverse direction, we regard the dynamic yield stress as that obtained through quasi-static test. Also, when defining the constitutive equation in ABAQUS, we did not use strain-rate-dependent model. Instead, the constitutive equation in high strain rate is defined as that in quasi-static test.

4.2.2 Dynamic Yield Stress in the Radial Direction

The dynamic yield stress in the axial direction of the specimens (also the rolling direction of the sheet) is estimated through Equation (4-8). Based on the strain-rate-insensitive property, the dynamic yield stress in the transverse direction is

determined by quasi-static test. However, the dynamic yield stress in the short-transverse direction can not be determined by the quasi-static test, since the thickness of the sheet is only 8 mm. In this section, we solve the problem according to anisotropic plasticity.

The deformed specimen is divided into segments by the intervals of CMM measuring points. Consider a sliced segment like $A_f B_f$ in Figure 4.9(a). It is assumed to be truncated ellipse cone (Figure 4.9(b)). In Figure 4.9(c), this ellipse frustum is transformed into an ellipse cylinder with the same height. r_a^i, r_a^{i+1}, r_b^i, r_b^{i+1} and h^i are obtained from the measurement. After the shape transformation, the major and minor radii of the equivalent ellipse cylinder are:

$$\begin{cases} \bar{r}_a^i = \dfrac{1}{\sqrt{3}}\left(r_a^{i+1^2} + r_a^{i+1} r_a^i + r_a^{i^2}\right)^{\frac{1}{2}} \\ \bar{r}_b^i = \dfrac{1}{\sqrt{3}}\left(r_b^{i+1^2} + r_b^{i+1} r_b^i + r_b^{i^2}\right)^{\frac{1}{2}} \end{cases}. \tag{4-11}$$

The conservation of volume is applied during the transformation. The plastic radial strains in the major and minor directions are:

$$\begin{cases} \varepsilon_a^p = \ln\left(\bar{r}_a^i / r_0\right) \\ \varepsilon_b^p = \ln\left(\bar{r}_b^i / r_0\right) \end{cases}. \tag{4-12}$$

r_0 is the radius of the un-deformed specimen.

The ratio of plastic radial strain is obtained through $\varepsilon_a^p / \varepsilon_b^p$. Figure 4.10 shows the relation between the ratio and the axial distance. All the data is collected in the barreling zone. It begins with compressive strain -16% and ends with -2%. Notice that the values of the axial distance are the length between the current point and the stating point (with -16% axial strain). In the figure, the strain ratios from different specimens

vary near 3.5. Considering the uniaxial compression state in the barreling regions, the constant ratios in the barreling zones imply that the shape of yield surface remains geometrically similar during the dynamic compression procedure, i. e, the yield surface expands proportionally. To avoid entering the mushroomed region, the data at higher compressive strain is not collected. The data at lower compressive strain is also avoided due to the slight variation of the radius in the un-deformed specimens. The dynamic yield stress can be determined with the association of Hill's criterion. Hill's yield criterion for an anisotropic material is

$$2f(\sigma_{ij}) = F(\sigma_y - \sigma_z)^2 + G(\sigma_z - \sigma_x)^2 + H(\sigma_x - \sigma_y)^2 + 2L\tau_{yz}^2 + 2M\tau_{xz}^2 + 2N\tau_{xy}^2 = 1 \quad (4\text{-}13)$$

F, G and H are parameters characteristic of the tensile or compressive yield stresses. They can be determined from the yield stresses in the corresponding directions. Here we orient the 2195-T8 aluminum-lithium alloy sheet with a coordinate in such a way that rolling that transverse and short transverse directions are parallel with x, y and z directions respectively (Figure 4.11). Assume that the yield stresses in the rolling, transverse and short-transverse directions are σ_r, σ_t and σ_{st}, respectively. The uniaxial loading condition in the three directions is given by:

$$\begin{cases} G\sigma_r^2 + H\sigma_r^2 = 1 \\ F\sigma_t^2 + H\sigma_t^2 = 1. \\ F\sigma_{st}^2 + G\sigma_{st}^2 = 1 \end{cases} \quad (4\text{-}14)$$

Solve the equations, we have

$$\begin{cases} F = \frac{1}{2}(-\frac{1}{\sigma_r^2}+\frac{1}{\sigma_t^2}+\frac{1}{\sigma_{st}^2}) \\ G = \frac{1}{2}(\frac{1}{\sigma_r^2}-\frac{1}{\sigma_t^2}+\frac{1}{\sigma_{st}^2}) \\ H = \frac{1}{2}(\frac{1}{\sigma_r^2}+\frac{1}{\sigma_t^2}-\frac{1}{\sigma_{st}^2}) \end{cases} . \tag{4-15}$$

In Hill's criterion, $f(\sigma_{ij})$ can also be regarded as a plastic potential [14]. Using the normality flow rule associated with the plastic potential function $f(\sigma_{ij})$, the incremental plastic strain can be derived as

$$d\varepsilon_{ij}^p = d\lambda \frac{\partial f}{\partial \sigma_{ij}}, \tag{4-16}$$

where $d\lambda$ is a proportionality factor. Substitute Equation (4-13) into Equation (4-16), we have the incremental plastic strains in the rolling, transverse and short transverse directions:

$$\begin{cases} d\varepsilon_r^p = d\lambda(G(\sigma_r-\sigma_{st})+H(\sigma_r-\sigma_t)) \\ d\varepsilon_t^p = d\lambda(F(\sigma_t-\sigma_{st})+H(\sigma_t-\sigma_r)) \\ d\varepsilon_{st}^p = d\lambda(F(\sigma_{st}-\sigma_t)+G(\sigma_{st}-\sigma_r)) \end{cases} . \tag{4-17}$$

Only the component σ_r exists due to the uniaxial compression. Equations (4-16) reduce to

$$\begin{cases} d\varepsilon_r^p = d\lambda(G+H)\sigma_r \\ d\varepsilon_t^p = d\lambda(-H)\sigma_r \\ d\varepsilon_{st}^p = d\lambda(-G)\sigma_r \end{cases} , \tag{4-18}$$

and the proportional loading characteristic enables us to integrate Equations (4-18) to get:

$$\begin{cases} \varepsilon_r^p = \lambda(G+H)\sigma_r \\ \varepsilon_t^p = \lambda(-H)\sigma_r \\ \varepsilon_{st}^p = \lambda(-G)\sigma_r \end{cases} . \tag{4-19}$$

According to Figure 4.10, the ratio of major and minor radial plastic strain is 3.5.

Therefore,

$$\frac{\varepsilon_t^p}{\varepsilon_{st}^p} = \frac{H}{G} = 3.5 . \tag{4-20}$$

Rewriting H and G with Equation (4-16), we relate the axial strength with the radial strength as

$$\frac{\frac{1}{\sigma_r^2} - \frac{1}{\sigma_t^2} + \frac{1}{\sigma_{st}^2}}{\frac{1}{\sigma_r^2} + \frac{1}{\sigma_t^2} - \frac{1}{\sigma_{st}^2}} = 3.5 . \tag{4-21}$$

As discussed above, 2195-T8 aluminum-lithium alloy is insensitive of strain rate. Therefore, dynamic yield stresses in the rolling and transverse direction are taken to be $\sigma_r = 610\ MPa$ and $\sigma_t = 565\ MPa$ (according to Figure 3.6). Solving Equation (4-21), we get the dynamic yield stress in the short transverse direction $\sigma_{st} = 465\ MPa$.

4.2.3. Finite Element Analysis of 2195-T8 Aluminum-Lithium Alloy Taylor Impact Test

4.2.3.1 Finite Element Modeling

The mesh of cylindrical specimen was produced in ABAQUS 6.9-1 and was refined with HYPERMESH 9.0. The mesh was mainly constructed of first order hexagonal elements (C3D8R). The pentagonal elements (C3D6) near the periphery of the specimens are generated by the refinement of HYPERMESH. More than 15,000 elements were used to model the cylinder. A small size of the elements is necessary for the simulation of the initiation and propagation of the cracks in the mushroom

region. A rigid surface composed of rectangular elements was fixed in space at the rigid body reference node, representing a non-compliant target. The cylindrical specimen model impacted the rigid surface at the same speeds as those in the experiment by apply initial velocity conditions to all the nodes in the mesh, and directing the velocity toward the simulated target. The calculations were performed for $90\,\mu s$, at which time the plastic deformation from the impact had ceased and transient stress waves had decayed.

The reference constitutive equation is defined by the quasi-static data in the rolling direction. Here we did not use the Johnson-Cook model due to the strain-rate-insensitive property of the 2195-T8 aluminum-lithium alloy. Constitutive equations in the transverse and short transverse direction are related to the reference one by scaling factor. Table 5 shows the six anisotropic plastic coefficients defined in POTENTIAL, ABAQUS. R_{12}, R_{13} and R_{23} are defined as 3 due to the lack of shear characteristics for the alloy. In the simulation, we examine the effect of these three coefficients by defining them as 2.778, 2.286.

During the impact, a fraction of plastic work is converted to heat. Since the impact event is rapid and does not allow much time for heat to be conducted away, the conditions are essentially adiabatic. The increase in the local temperature owing to plastic work is

$$\Delta T = \int \frac{\alpha}{\rho c_p} \sigma_{ij} d\varepsilon_{ij}^p \,, \tag{4-22}$$

where ρ, c_p, σ_{ij}, ε_{ij}^p are the material density, the specific heat, the components

of the stress and plastic strain respectively. α is the fraction of the plastic work converted to heat. Due to the low temperature sensitivity of the flow stress for 2195-T8 aluminum-lithium alloy, the change in the temperature of the specimens does not result in a significant change in the flow stress. We follow several open literatures and set $\alpha = 0.9$ [15][16]. The original temperature of the specimens is $298\,K$.

ABAQUS/Explicit offers two methods to treat failed elements. One method is that failed elements are completely removed from the calculation. The other method is that failed elements are still capable of holding pressure, but not shear or tension. Both techniques are tried in our simulation, and they give very close results. Therefore, we choose the first way to reduce computational efforts.

4.2.3.2 Anisotropic Taylor impact without fracture

Figure 4.12 shows the finite element simulation of the Taylor impact specimen. The impact speed is $190\,m/s$. Comparing with Figure 3.1, we can see that the shape of the specimen obtained in the simulation is very close to that in experiment. The constitutive equation is defined through quasi-static data. The coefficients of anisotropic plasticity in POTENTIAL are listed in Table 5. The tension coefficients in the table are obtained through the yield strength in the corresponding directions. The shear coefficients are defined as 3 as in the isotropic material. Since the Taylor impact test is mainly uniaxial compression, the influence of shear coefficients is limited. To test the influence, we also set the shear coefficients equal 2.286 and 2.778. They gave almost identical specimen shape.

As stated in Chapter 4.1, the strain state in the barreling region is uniaxial compression for isotropic material. Here we examine the validity of this conclusion for anisotropic material. Figure 4.13 is the distributions of logarithmic strain in radial direction in major and minor side. It can be seen that the strain distribution is uniaxial (the striated pattern of strain distribution) in the minor side deformation. But in the major side deformation, the strain varies at a fixed axial position. It means the strain distribution in the barreling region is not pure uniaxail compression. More plasticity analysis on anisotropic Taylor impact model can be found in Maudlin et al. [17].

3.3 Anisotropic Taylor impact with fracture

In this section, the fracture of the material in the mushroom region of an anisotropic Taylor impact test is analyzed for the first time. The dependencies that affect the fracture are analyzed according to removing elements with corresponding characteristics in the post-test results. Notice that we did not perform the simulation of the fracture due to the lack of material failure coefficients for 2195-T8 aluminum-lithium alloy in the open literature.

The prediction of material fracture in uncracked bodies is currently a technical challenge. Strain rate, temperature, stress triaxiality, equivalent stress and strain can effect the initiation and propagation of the fracture. A lot of criteria are provided to predict to initiation of fracture [18]. Most of these failure criteria are phenomenological. They control the onset of fracture through the equivalent fracture

strain, i. e. the material will fail once the equivalent fracture strain reaches a critical value. This inspires us to determine the dependencies of the fracture by removing elements with corresponding characteristics higher than a critical value. If the position of the elements removed coincides with the fracturing position, we conclude that the characteristic is a dependency of the fracture.

As shown in Figure 3.1(d) to (f), the fracture happens in the weaker side of the specimen. The angle of the fracture surface to the loading direction is about 45°. This means a shear fracture may exist. However, the fracture differs from traditional one by showing the V-shaped surfaces. This difference implies the existence of dependencies other than maximum shear stress.

Figure 4.14 explores the influence of the maximum shear stress by showing the appearance of the specimen after removing the elements with maximum shear stress higher than $190\,MPa$. The removed elements are in the transition area between the mushroom and barreling region with an angle about 45° to the loading direction. Compared with the photo of fractured specimens, we can see that the position and angle of the removed elements are close to the fracture in Figure 3.1(d). This demonstrates the association between the maximum shear stress and the fracture. The weakness of this maximum shear stress criterion is that it cannot explain why the propagation of the fracture is from the impact surface to the transition of mushroom and barreling region [19]. If we assume that the fracture will happen at the point with maximum shear stress, the transition region will fracture first, which is not true

according to the observation in the test.

Figure 4.15 shows the appearance of the specimen after removing the elements with the equivalent plastic strain higher than 0.44. Again, this figure is very like Figure 3.1(d), the fractured specimen. This similarity implies a dependency of fracture on the equivalent plastic strain. This test is motivated by the constant equivalent strain criterion [18], which states that fracture occurs in a point when the equivalent plastic strain reaches a critical value. However, when comparing Figure 3.1(f) with Figure 4.15, we can find out that the fracture does not happen at the central part of the impact surface although it has a higher equivalent plastic strain (or Von Mises stress). This is due to the low stress triaxiality in this region (Figure 4.16). Several criteria [18] show an increasing equivalent fracture strain as the stress triaxiality goes negative.

CHAPTER 5 CONCLUSIONS AND FUTURE WORK

An initial investigation regarding CMM based calculations of plastic strain distributions in Taylor impact specimens is made in this paper. These calculations are particularly well-suited to model strain in the barreling region. The assumptions of the simplified calculation method rely on the conservation of volume and an accurately measured deformed specimen profile. Additional simplification was made based on the axisymmetric deformation pattern of the deformed specimen. The CMM based calculation of plastic strain can be applied to specimens of different sizes, impact speeds, and at CMM various measurement intervals. The calculations were compared with a finite element model, and the comparison agreed very well in the barreling region of the specimen. This indicates that this experimental strain field determination method can be used to validate material modeling coefficients. In the present form, the simplified calculation method can not accurately calculate surface strains in the mushroom region of the impacted specimen. This is due to the existence of a complex multiaxial stress state leading to a non-uniform strain distribution on the cross-section of the specimen.

The high strain rate properties and the fracture of anisotropic material 2195-T8 aluminum-lithium alloy is studied using Taylor impact test. It found that the 2195-T8 aluminum-lithium aluminum alloy has low sensitivity in strain rate. The dynamic

yield stresses are determined in all three directions-longitudinal, transverse and short transverse. Based on the stresses calculated, material coefficients in Hill's criterion are obtained. Finite element simulation was performed. The fracture occurred in the mushroomed region is shear failure. Removing the elements with status higher than a critical value, the fracture dependencies are explored. Maximum shear stress, equivalent plastic strain and stress triaxiality are dependencies in the fracture of anisotropic Taylor impact test.

REFERENCES

[1] Taylor, G. I., 1948. The use of flat-ended projectiles for determining dynamic yield stress I. Theoretical consideration. Proc. Royal Soc. London A194 (1038), 289-299.

[2] Jones, S. E., Gillis, P. P., On the equation of motion of the un-deformed section of a Taylor impact specimen. J. Appl. Phys. (1987) 64 (12), 6699-6712.

[3] Jones, S.E, Drinkard, J. A., Rule, W. K., Wilson, L. L., An elementary theory for the Taylor impact test. Int. J. Impact Eng. (1998) 21,1-13.

[4] Jones, S.E., Maudlin, P., J., Foster, J. C., An engineering analysis of plastic wave propagation in the Taylor test. Int. J. Impact Eng. Vol. 19, No. 2, pp. 95-106, (1997).

[5] Russo, R., Dutton, N., Baker, B., Tones, K., Jones, S., E. and Brewster, R. A.., Taylor cylinder testing of high strength steels for hard target warhead applications. Proceedings of ASME PVP 2009, Czech Republic, PVP 200977037.

[6] Brünig, M, Driemeiter, L., Numerical simulation of Taylor impact test. International Journal of Plasticity 23 (2007) 1979-2003.

[7] Banerjee, B., Taylor Impact Tests: Detailed Report. Report No. C-SAFE-CD-IR-05-001.

[8] Foster, J. C., Maudlin, P. J., and Jones, S. E., On the Taylor test: A continuum analysis of plastic wave propagation. Proc. 1995 APS Topical Conf. on shock compression of condensed matter, Seattle, WA(1995).

[9] L. De Chiffre, H.N. Hansen, R.E. Morace,. Comparison of coordinate measuring machines using an optomechanical hole plate. CIRP Annals-Manufacturing Technology. Volume 54(2005), Issue 1, Pages 479-482

[10] Abbe, M., Takamasu, and Ozono, K., Reliability on calibration of CMM. Measurement 33 (2003) 399-368.

[11] Cauchick-Miguel, P., Kinga, T. and Davis, J., CMM verification: a survey. Measurement 17(1)(1996) 1-16.

[12] Johnson, G. R., Cook, W. H., 1983. A constitutive model and data from metals subjected to large strains, high strain rates and high temperatures. In: Proc. 7th International Symposium on Ballistics. pp. 541-547.

[13] L. Djapic Oosterkamp, A. Ivankovic, G. Venizelos, High strain rate properties of selected aluminium alloys. Materials Science and Engineering A278 (2000) 225–235.

[14] Barkey, M. E., Socie, D., F., and Hsia, K., J., A yield surface approach to the estimation of notch strains for proportional and nonproportional cyclic loading. ASME Journal of Engineering Materials and Technology. 116:173-180, 1994.

[16] Plunkett, B., Cazacu, O., Lebensohn, R., A., Barlat, F., Elastic-visoplastic anisotropic modeling of textured metals and validation using the Taylor cylinder impact test. International Journal of Plasticity 23 (2997) 1001-1021.

[16] Kapoor, R., Nemat-Nasser, S., Determination of temperature rise during high

strain rate deformation. Mechanics of Materials 27 (1998) 1-12.
[17] Maudlin, P., J., Gray, G., T., Cady, C., M., Kaschner, G., C., High-Rate material modeling and validation using the Taylor cylinder impact test. Philosophical Transactions: Mathematical, Physical and Engineering Sciences, Vol. 357, No. 1756, Deformation Processing of Metals (Jun. 15, 1999), pp. 1707-1729.
[18] Wierzbicki, T., Bao, Y., Lee, Y., Bai, Y., Calibration and evaluation of seven fracture models. International Journal of Mechanical Science 47(2005) 719-743.
[19] Wierzbicki, T., Teng, X., Hiermaier, S., Rohr, I., Numerical prediction of fracture in the Taylor test. International Journal of solids and structures 42(2005) 2929-2948.

Table 1. Hardness Measurements of the copper alloy.

	Longitudinal	Transverse Vertical	Transverse Horizontal
Average Hardness (Knoop Hardness 50g)	123	126	124

Table 2. Parameters used in the Johnson-Cook model for the copper alloy.

A (MPa)	B (MPa)	C	n	m	$\dot{\varepsilon}_{p0}(/s)$	$T_0(K)$	$T_m(K)$
50	282	0.025	0.31	1.09	1.0	294	1356

Table 3. β of the copper alloy.

	4%	8%	12%	16%
β	0.94	0.91	0.85	0.82

Table 4. β of the 2195-T8 aluminum-lithium alloy.

	4%	8%	12%	16%
β	0.93	0.83	0.70	0.55

Table 5. Coefficients of anisotropic plasticity in POTENTIAL.

R_{11}	R_{22}	R_{33}	R_{12}	R_{13}	R_{23}
1	0.926	0.762	3	3	3

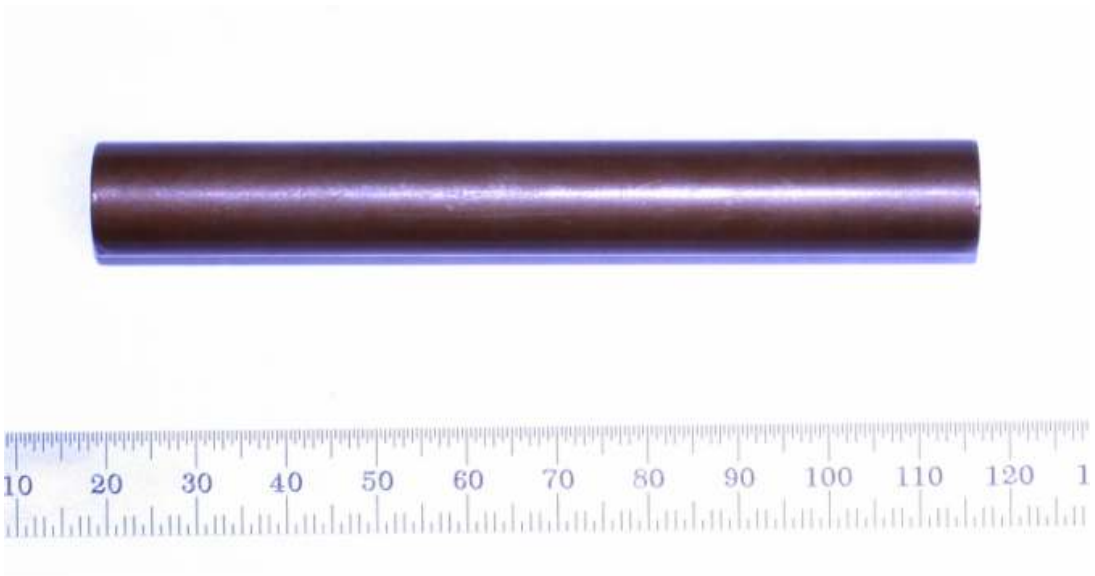

(a)

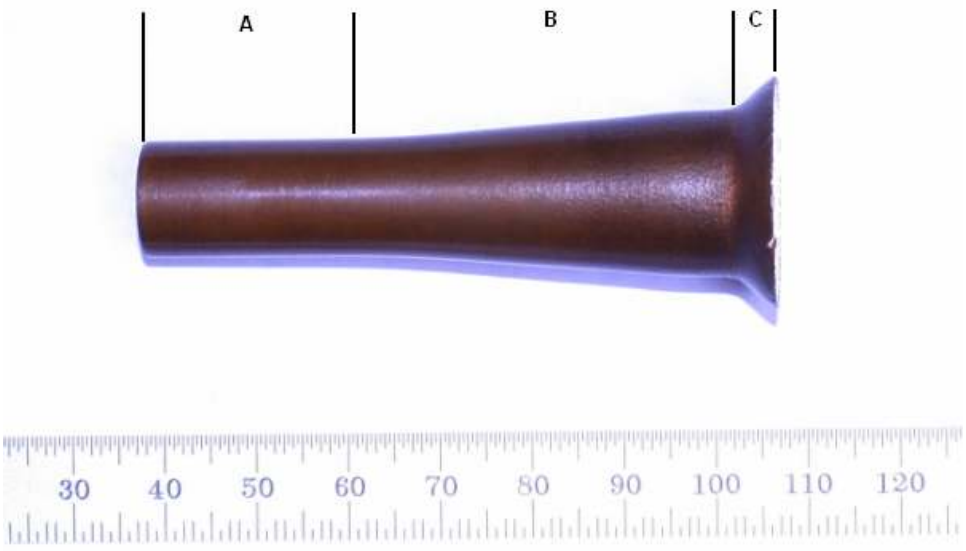

(b)

Figure 2.1. (a) An un-deformed 12 *mm* -diameter specimen. (b) A deformed 12 *mm* -diameter specimen (impact speed 195 m/s). A: elastic region, B: barreling region, C: mushroom region.

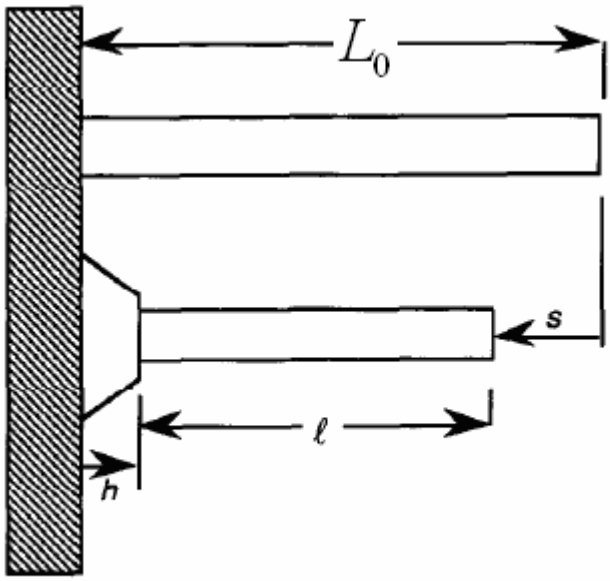

Figure 2.2. Schematic view of a Taylor specimen of original length L_0 which undergoes plastic deformation [4].

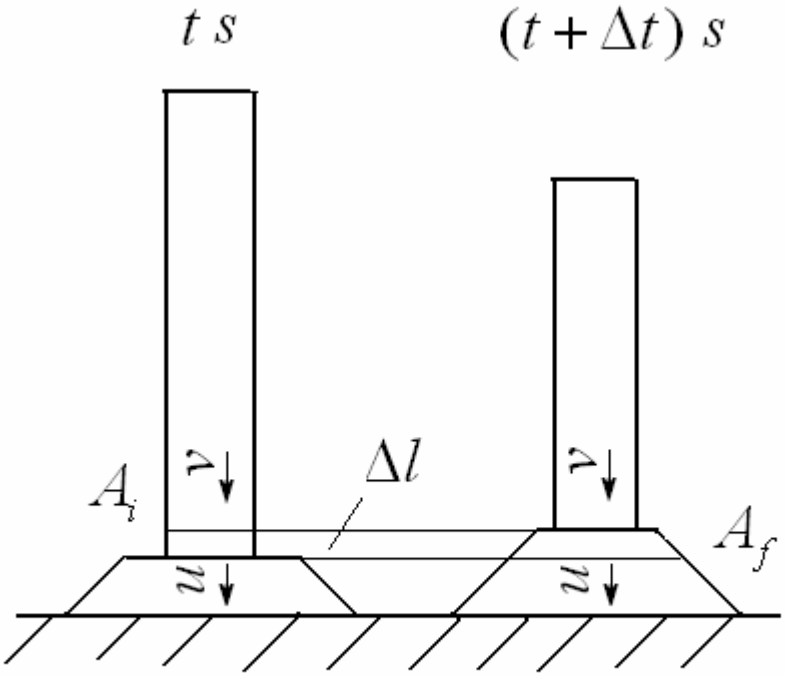

Figure 2.3. The deformation of an element over an elapsed time Δt. A_i and A_f are the cross-sectional areas before and after the impact respectively.

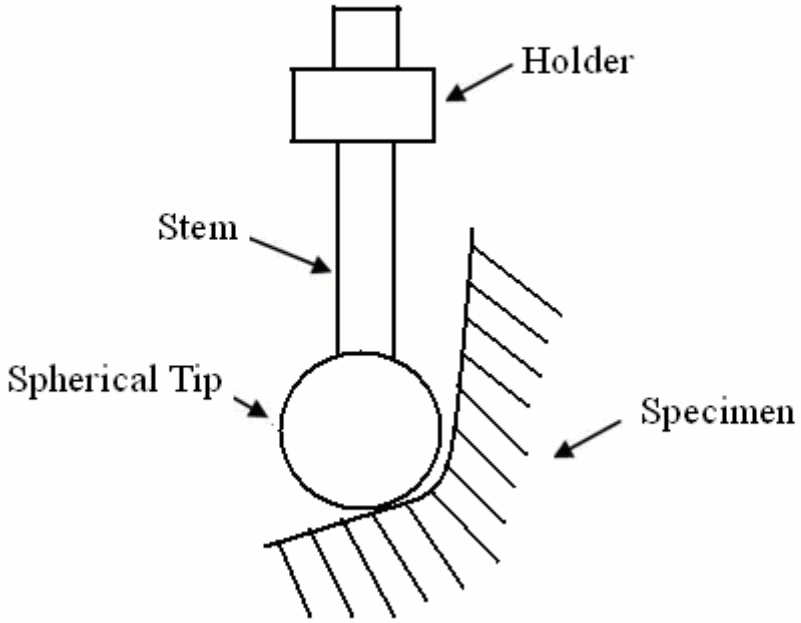

Figure 2.4. The influence of the radius of the spherical probe tip.

(a)

(b)

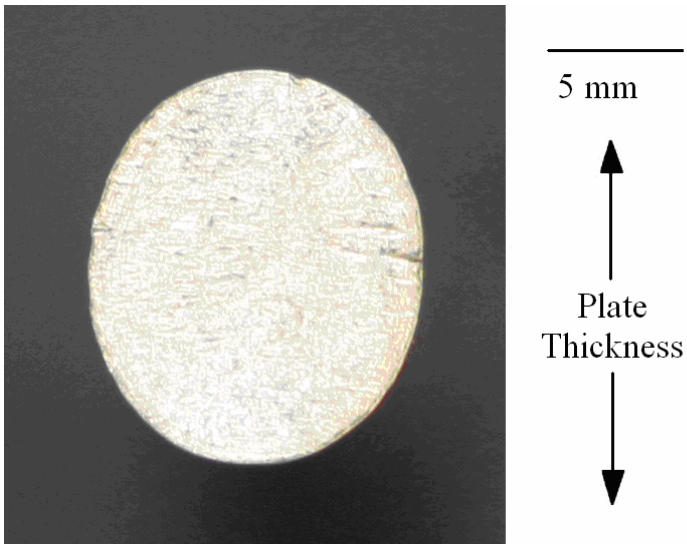

(c)

(d)

(e)

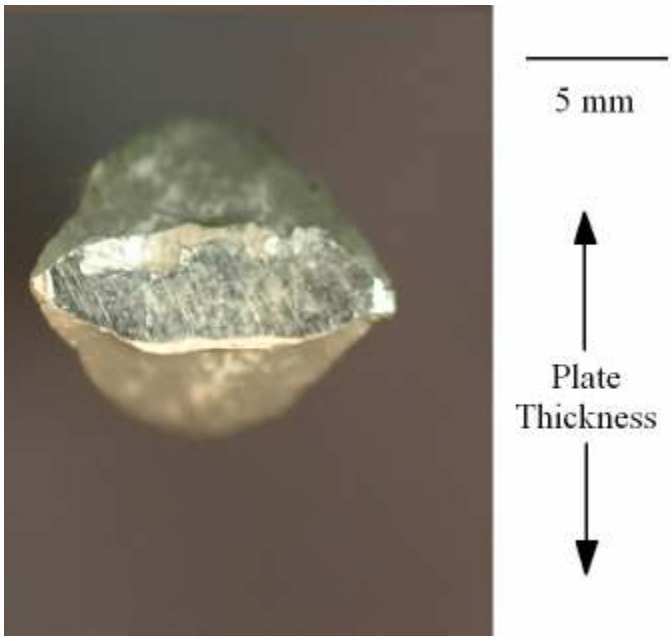

(f)

Figure 3.1. Photographs of the post-test Taylor impact specimens. All of the specimens were cut along the rolling direction. The impact speeds are (a)-(c), $186\,m/s$; (d)-(f), $221\,m/s$.

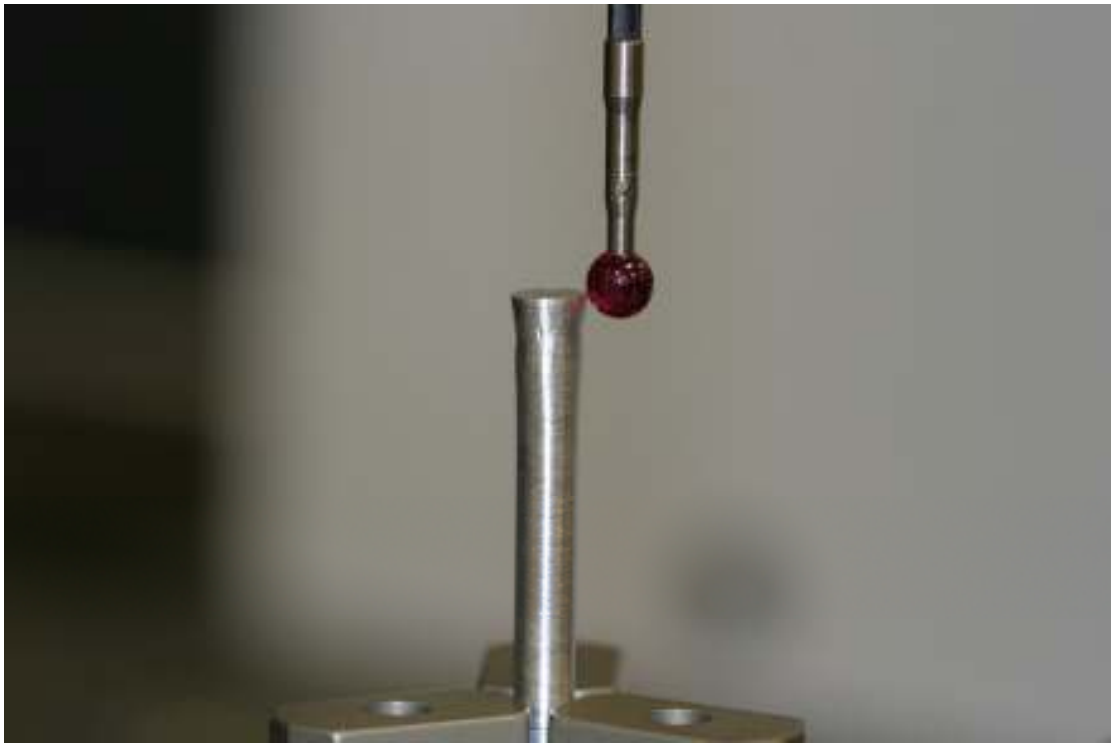

Figure 3.2. A coordinate measuring machine is measuring a deformed specimen.

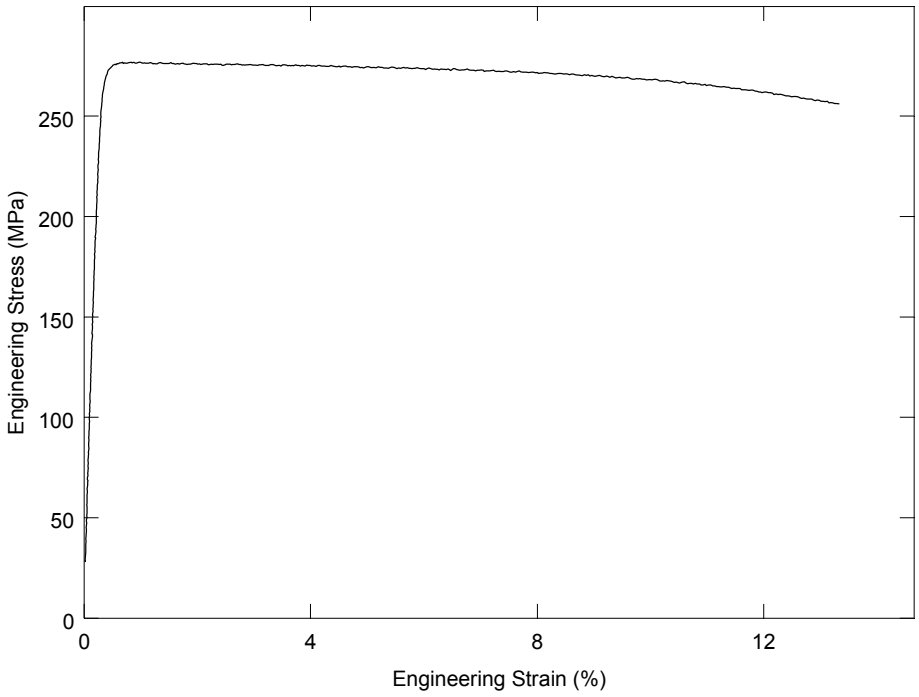

Figure 3.3. Quasi-static tension data for the copper alloy.

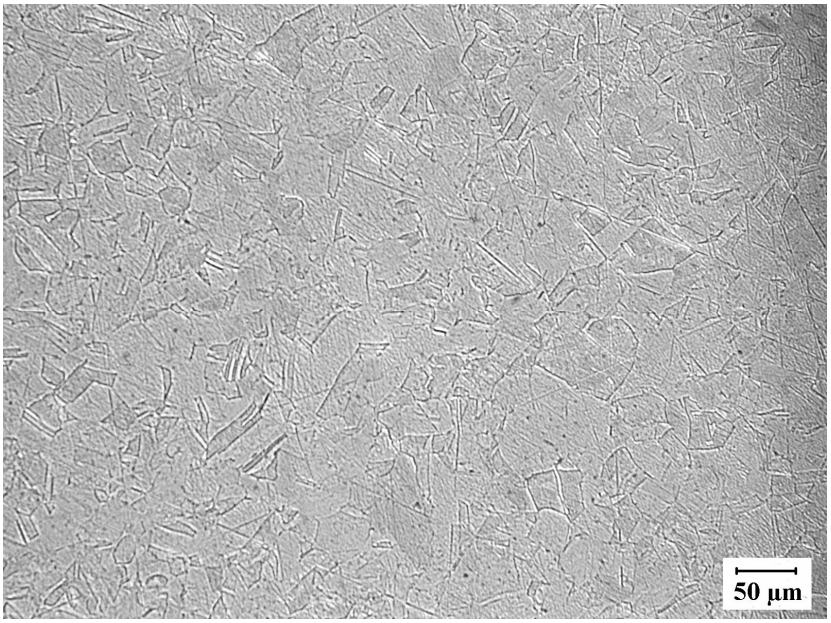

(a) Transverse

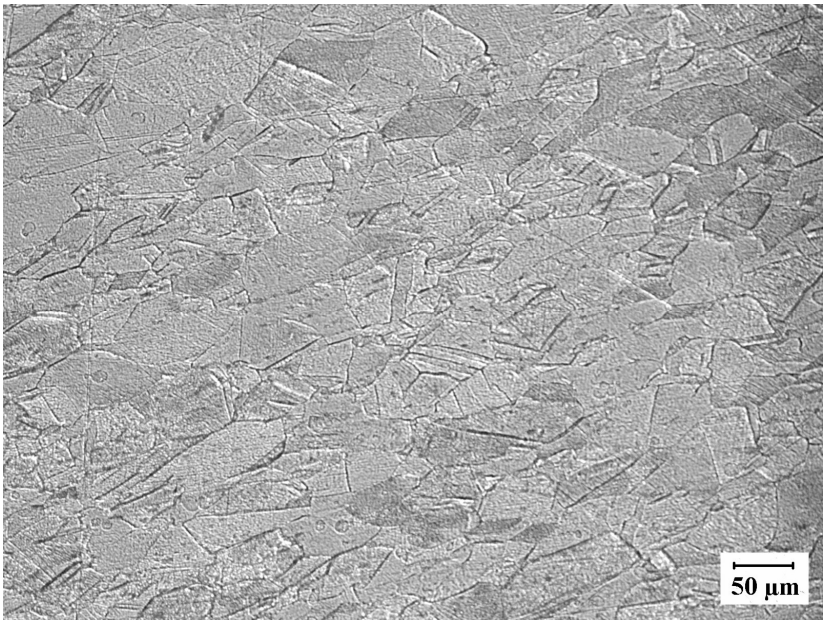

(b) Longitudinal

Figure 3.4. Microstructure of un-deformed copper specimen. Original Magnification 200x, Etch: 30% HNO_3 70% H_2O.

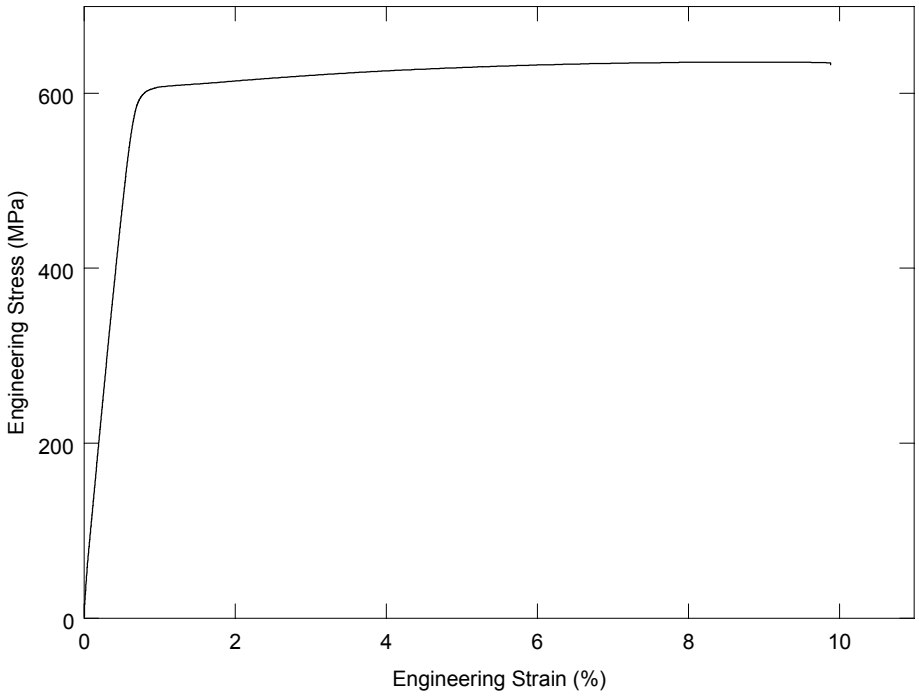

Figure 3.5. Quasi-static tension data for the 2195-T8 aluminum-lithium alloy in the rolling direction.

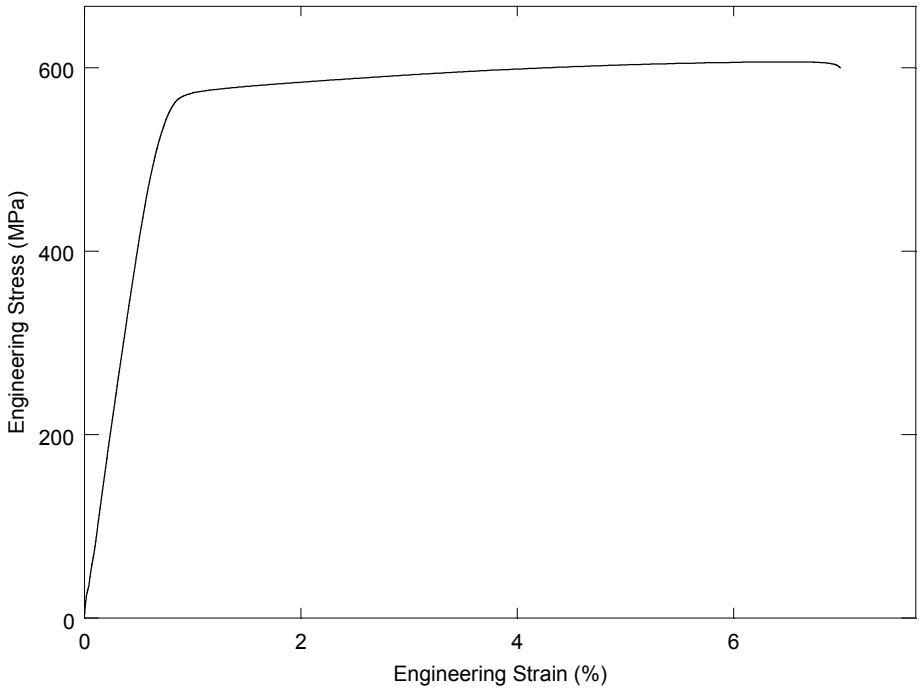

Figure 3.6. Quasi-static tension data for the 2195-T8 aluminum-lithium alloy in the transverse direction.

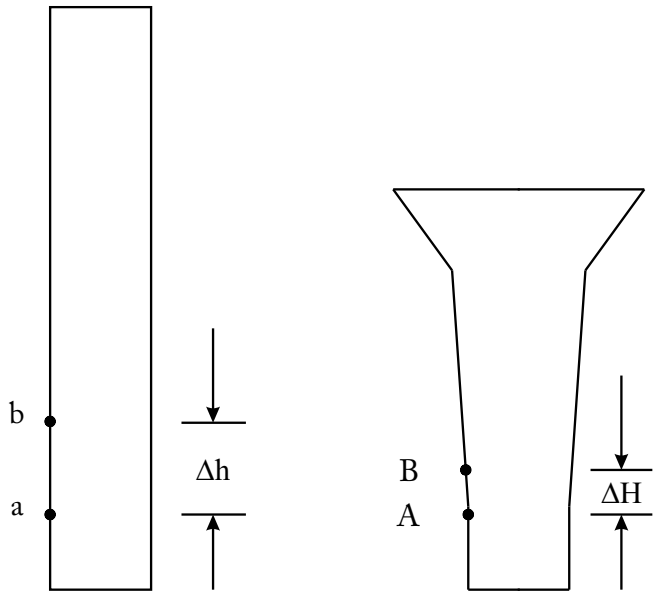

(a)

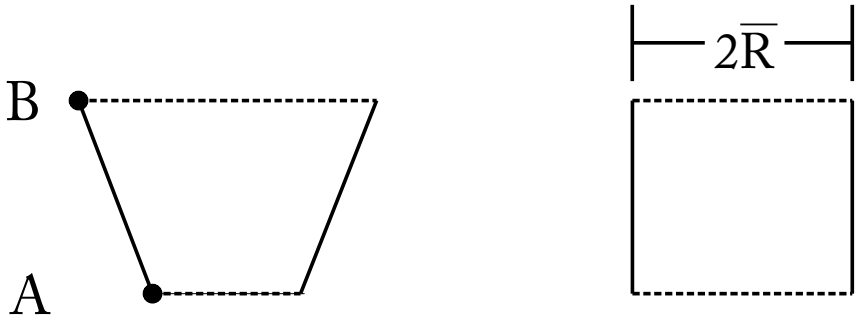

(b)

Figure 4.1. Schematic representation of (a) mapping of points a and b to the deformed specimen and (b) conversion of truncated cone segment to equivalent cylinder.

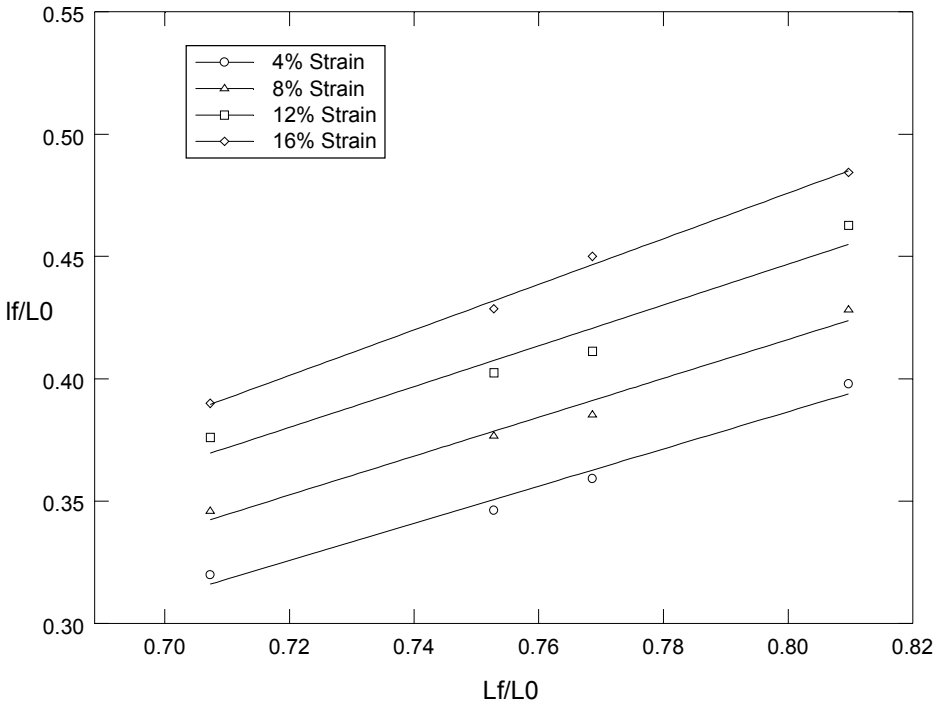

Figure 4.2. The results of the copper alloy.

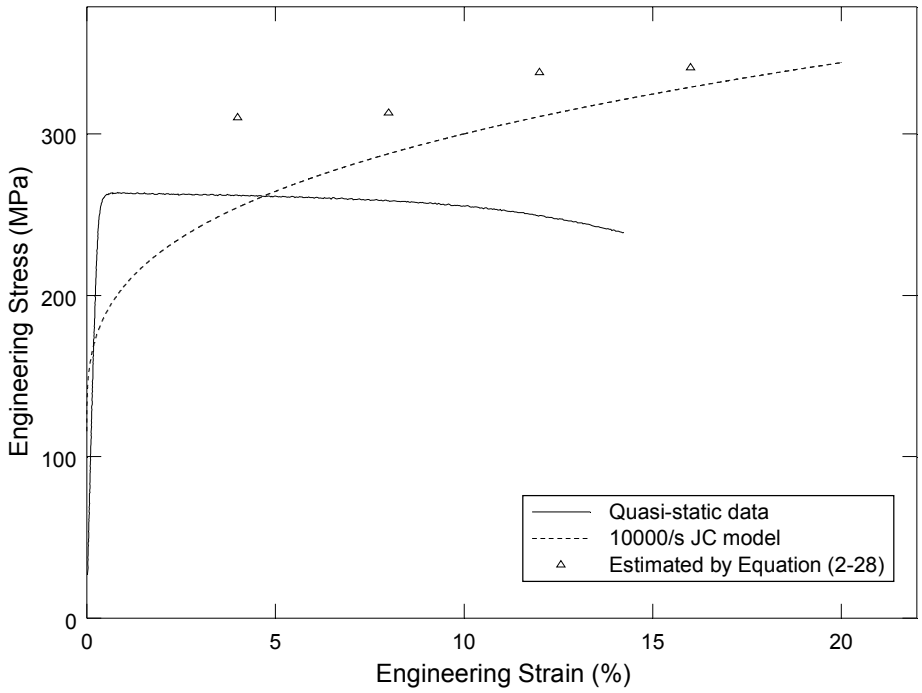

Figure 4.3. Comparison between quasi-static data, Johnson-Cook model and estimates of Equation (2-28).

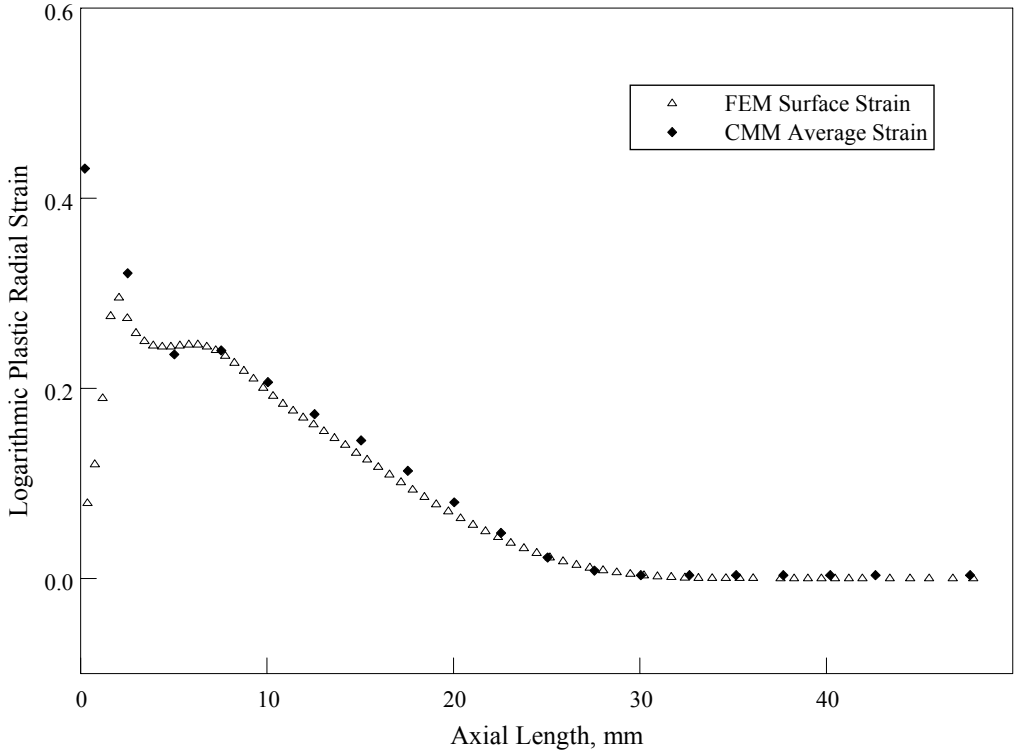
0.6
0.4
0.2
0.0
Logarithmic Plastic Radial Strain
FEM Surface Strain
CMM Average Strain
0
10
20
30
40
Axial Length, mm

(a)

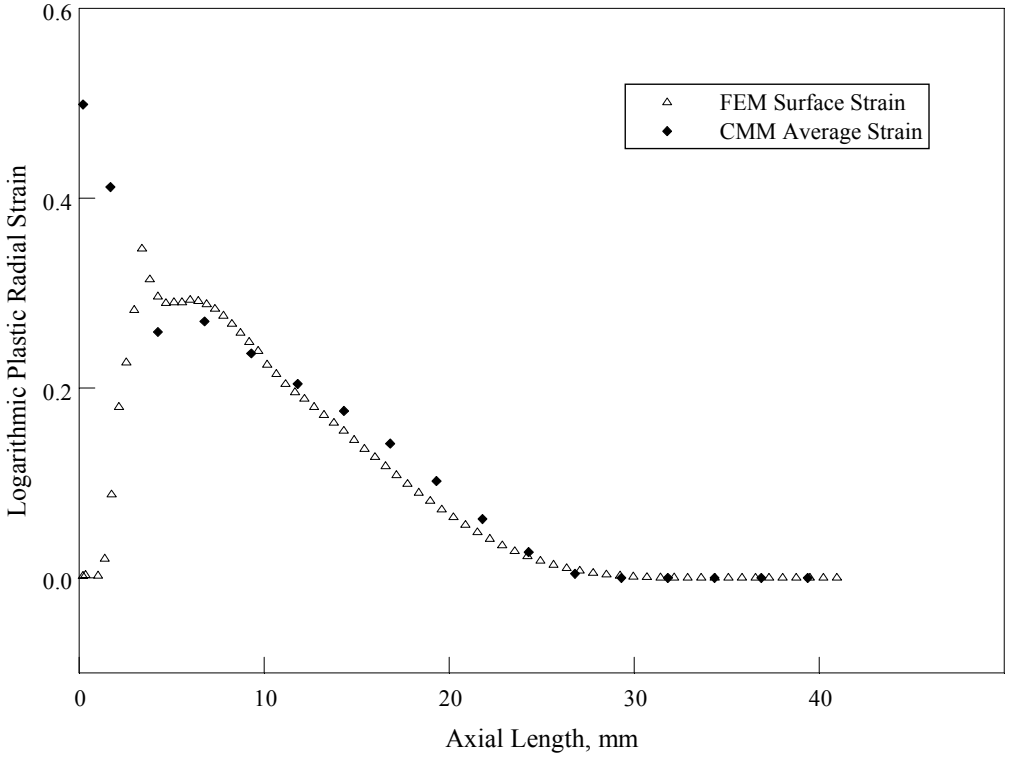
0.6
0.4
0.2
0.0
Logarithmic Plastic Radial Strain
FEM Surface Strain
CMM Average Strain
0
10
20
30
40
Axial Length, mm

(b)

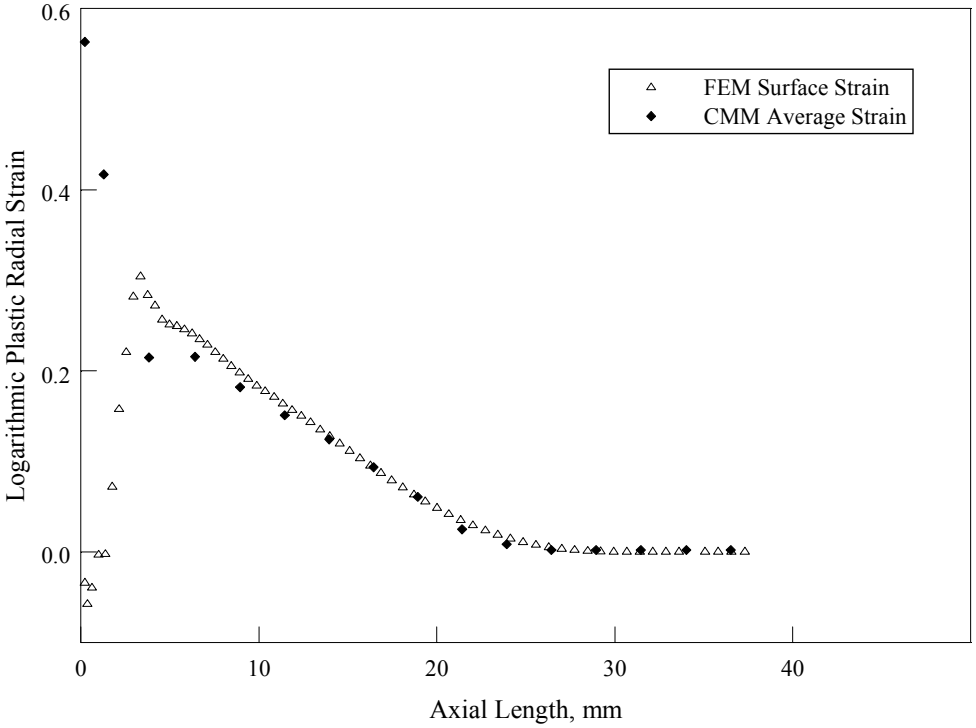
0.6
0.4
0.2
0.0
Logarithmic Plastic Radial Strain
FEM Surface Strain
CMM Average Strain
0
10
20
30
40
Axial Length, mm

(c)

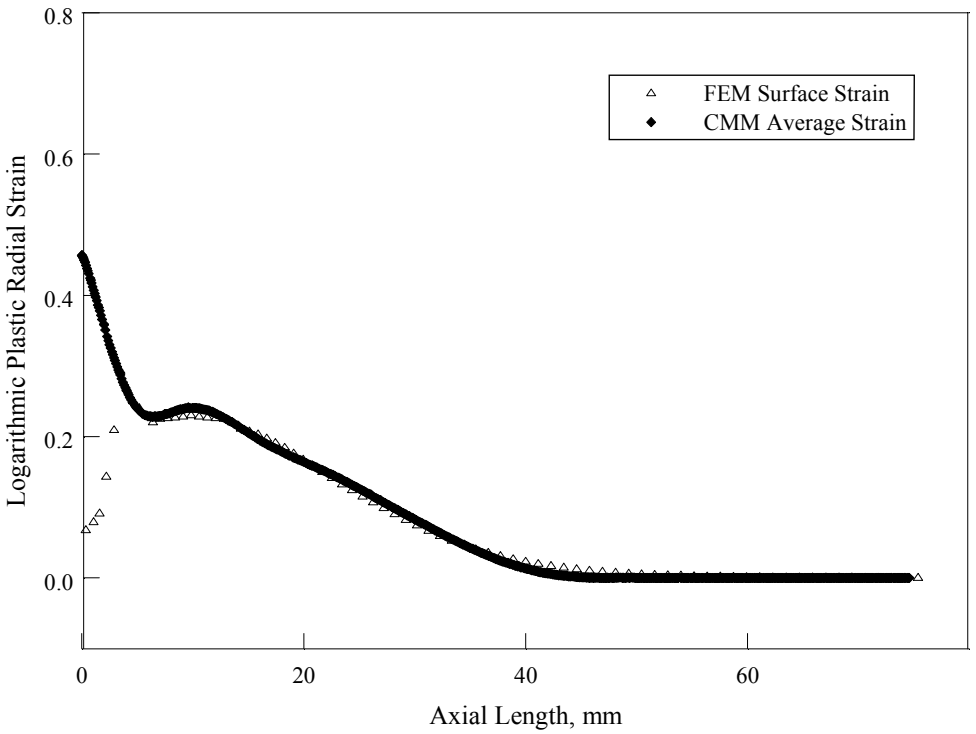
0.8
0.6
0.4
0.2
0.0
Logarithmic Plastic Radial Strain
FEM Surface Strain
CMM Average Strain
0
20
40
60
Axial Length, mm

(d)

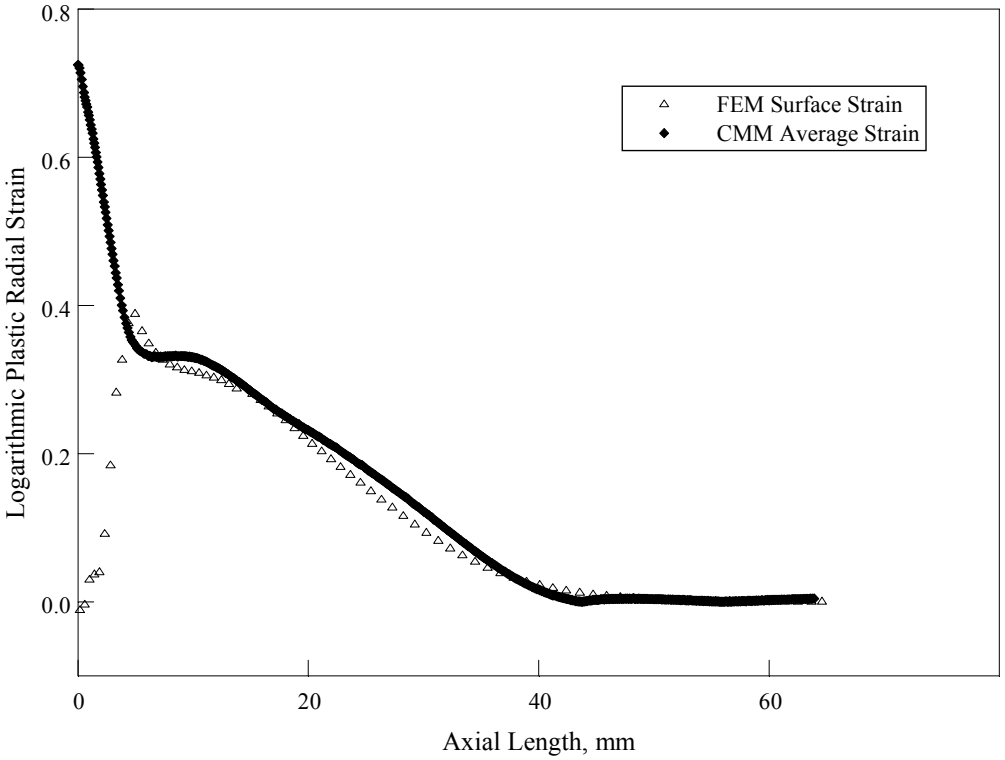

(e)

Figure 4.4. Logarithmic plastic radial strain distribution along the axial direction. (a), (b), and (c) are 7 mm-diameter specimens. (d) and (e) are 12 mm-diameter specimens. Their impact speeds are 153 m/s, 174 m/s, 197 m/s, 147 m/s, and 195 m/s.

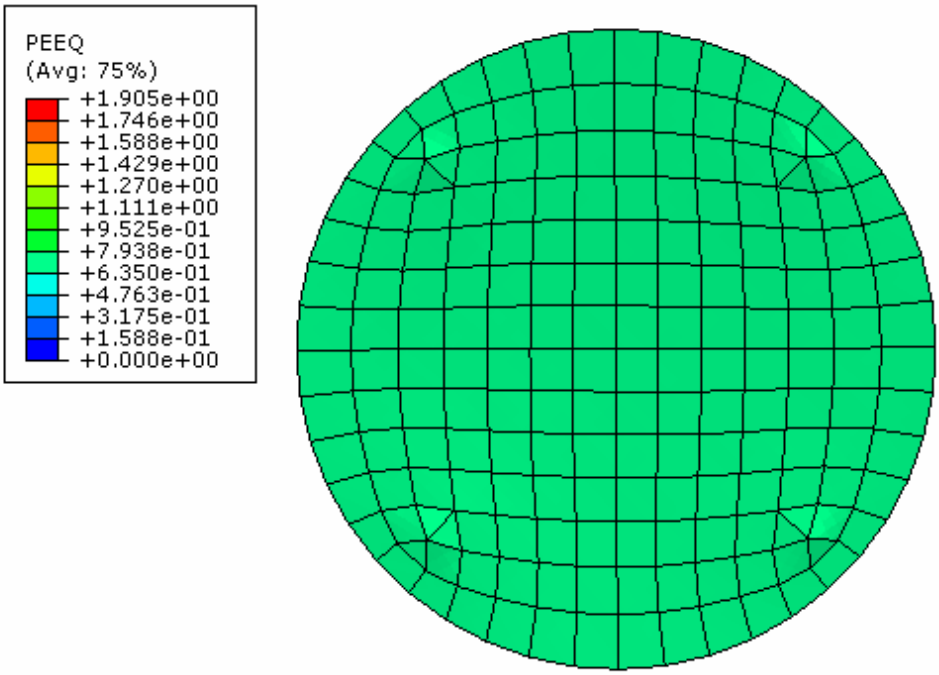

(a)

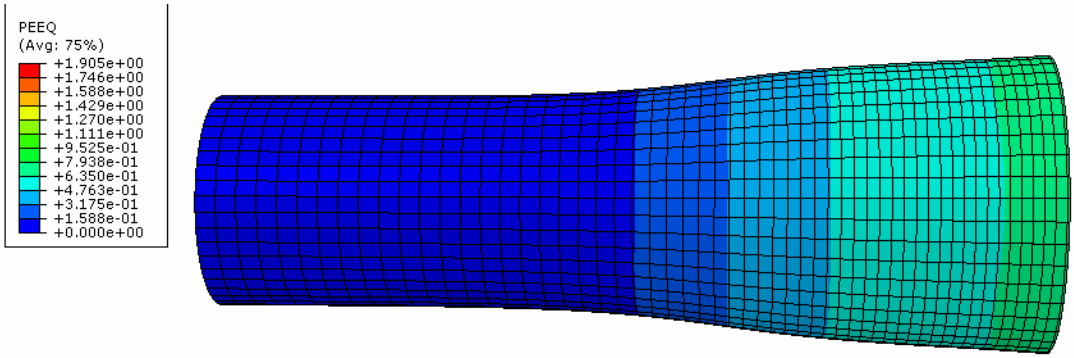

(b)

Figure 4.5. The distribution of equivalent plastic strain at 14.8 *mm* away from the impact surface (12 *mm* -diameter specimen, impact speed 195 m/s. PEEQ is equivalent plastic strain at integration points.). (a) Vertical view, (b) Profile view.

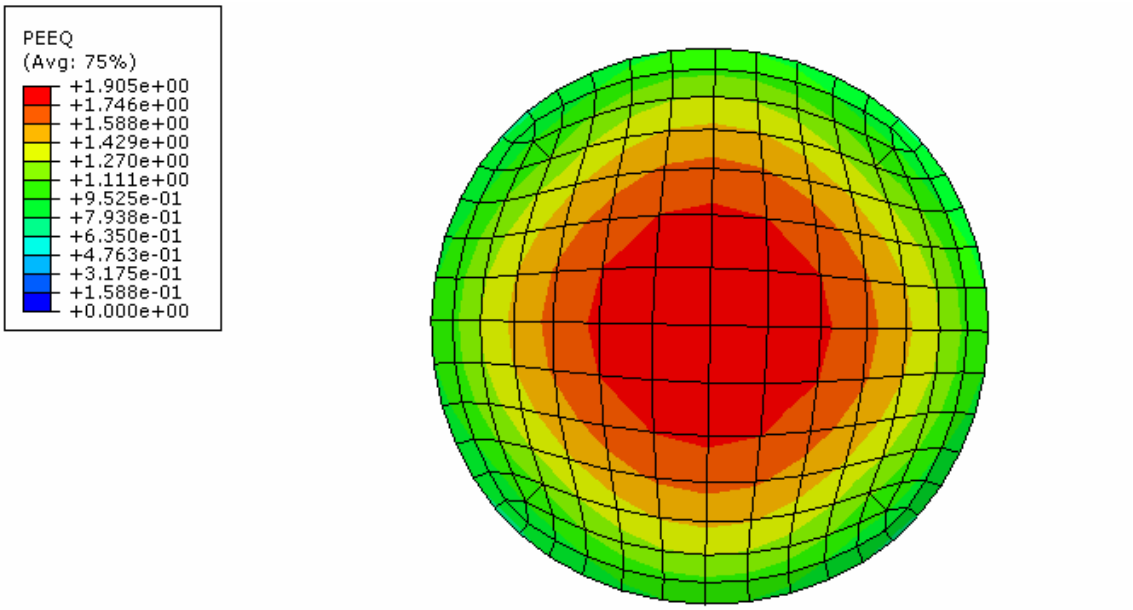

Figure 4.6. The distribution of equivalent plastic strain at the impact surface (12 *mm* -diameter specimen, impact speed 195 m/s . PEEQ is equivalent plastic strain at integration points. The triangular elements are generated during the mesh refinement to give a more axial symmetric deformation.).

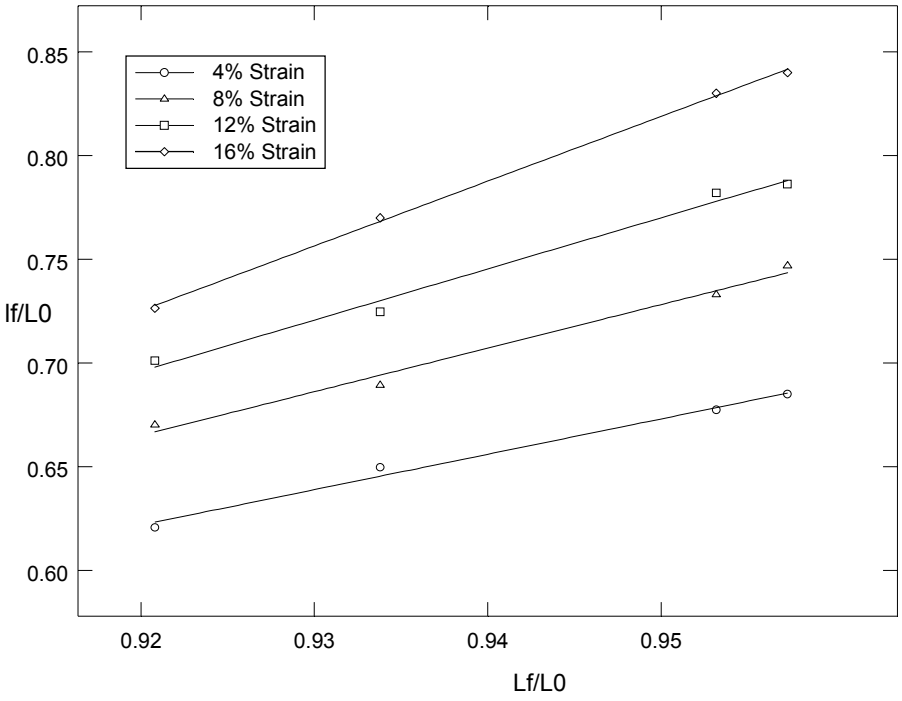

Figure 4.7. The results of the 2195-T8 aluminum-lithium alloy impact tests.

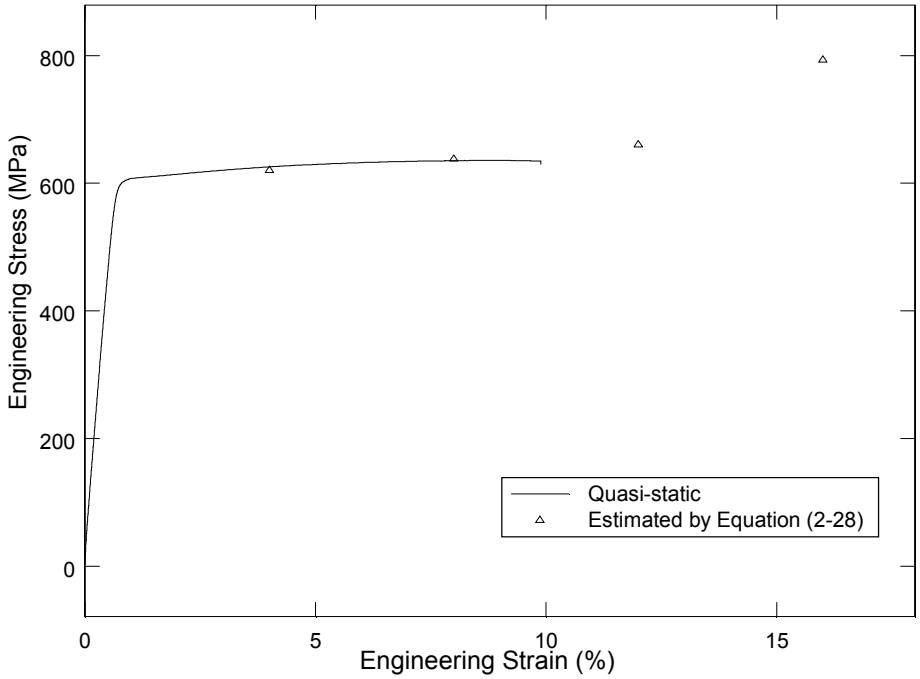

Figure 4.8. The comparison of the quasi-static data for 2195-T8 aluminum-lithium alloy and the dynamic yield stresses estimated by Equation (2-28).

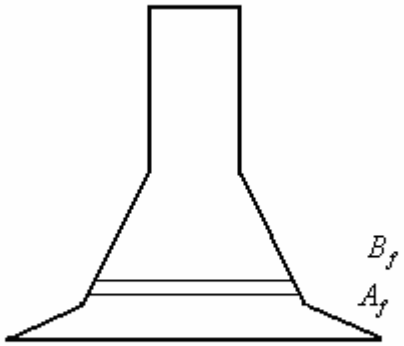

(a)

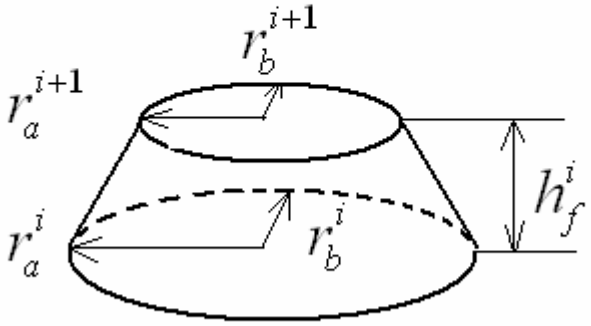

(b)

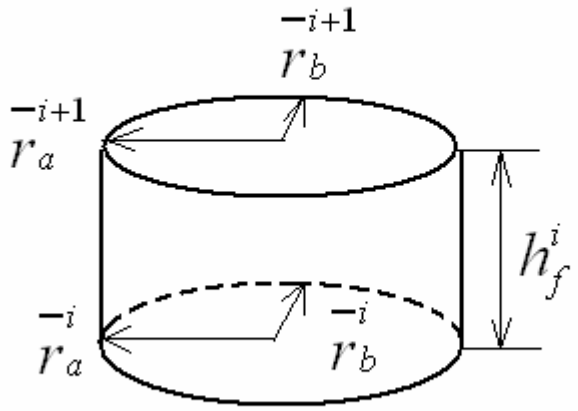

(c)

Figure 4.9. Schematic representation of conversion of a truncated elliptical conical segment to an equivalent ellipse.

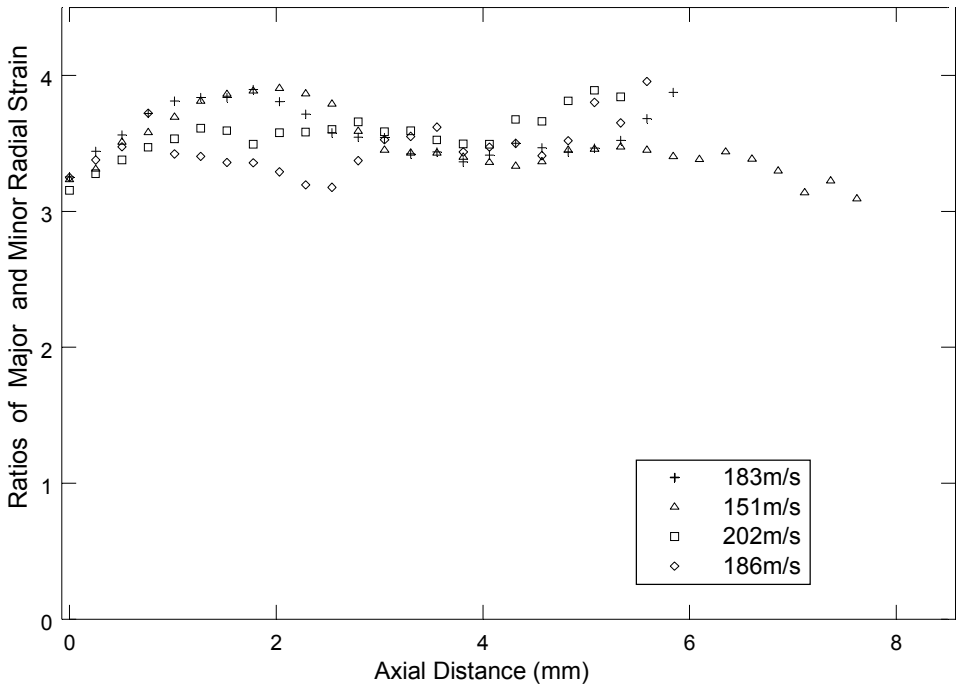

Figure 4.10. Ratios of major and minor radial strain in the barreling regions. These ratios are taken from specimens with varying impact speeds.

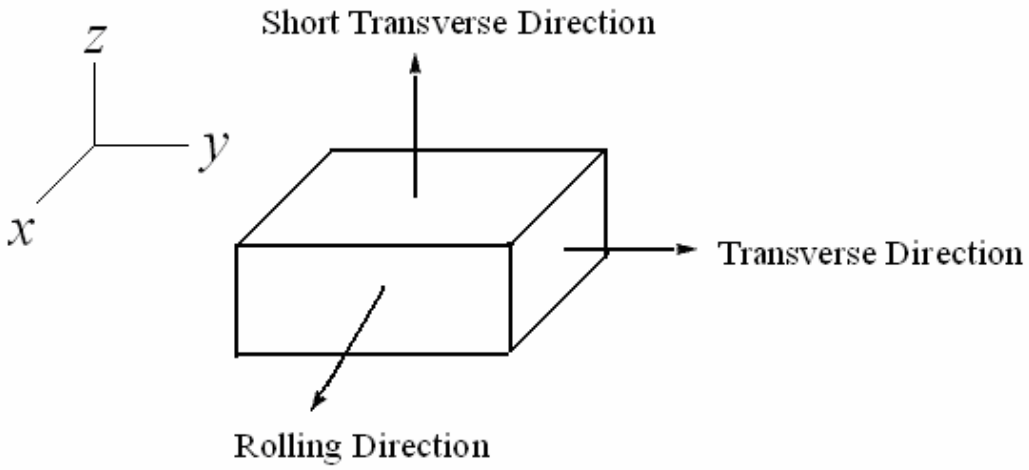

Figure 4.11. The orientation of the 2195-T8 aluminum-lithium alloy sheet in a Cartesian coordinate system.

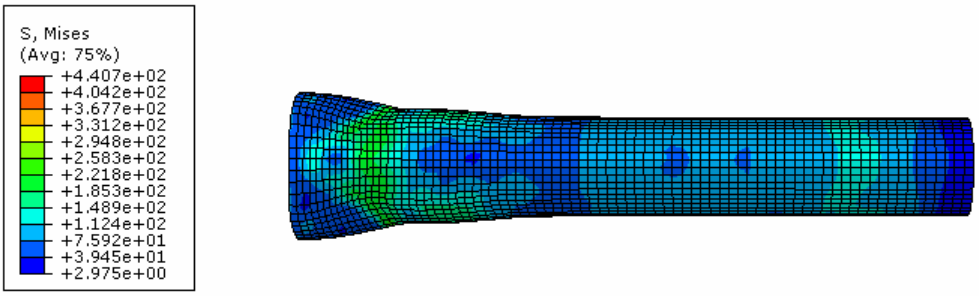

(a)

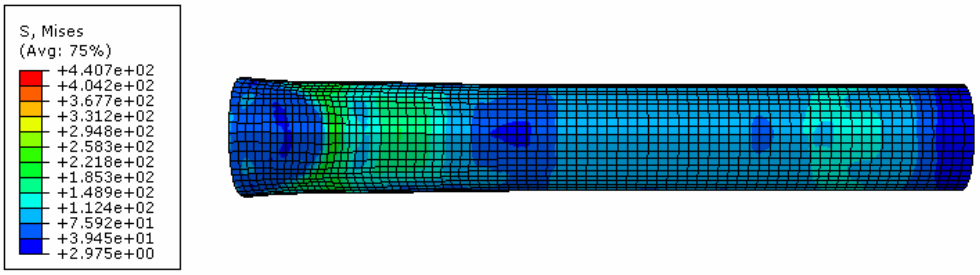

(b)

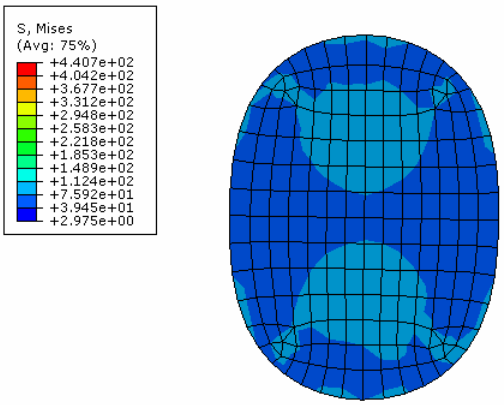

(c)

Figure 4.12. Finite element simulation of the Taylor impact specimen with a impact speed 190 m / s . (a) The major side deformation. (b) The minor side deformation. (c)

(c) The impact surface.

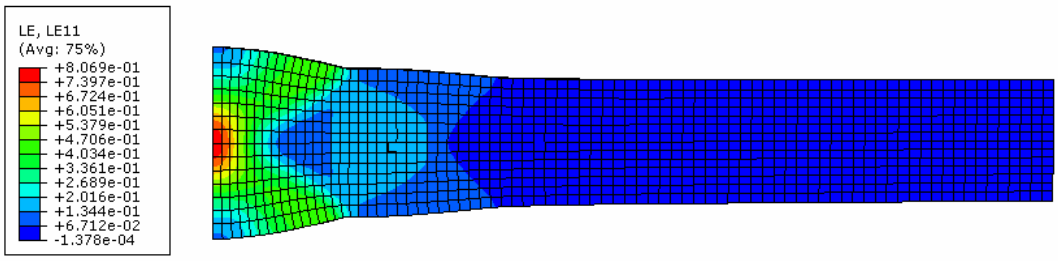

(a)

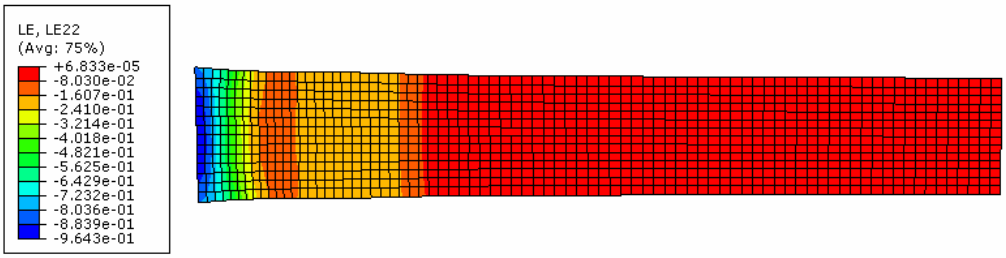

(b)

Figure 4.13. The distribution of logarithmic radial strain in the major (a) and minor sides (b).

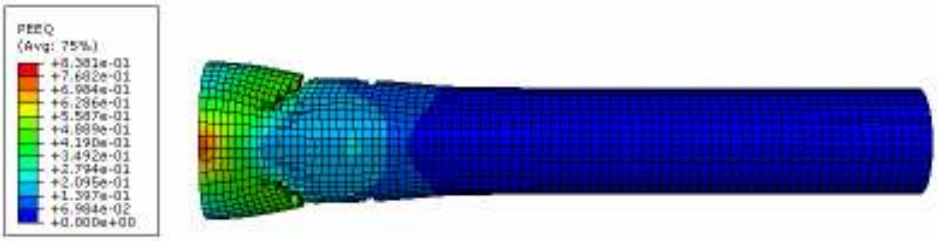

Figure 4.14. After removing elements with maximum shear stress higher than 190 MPa .

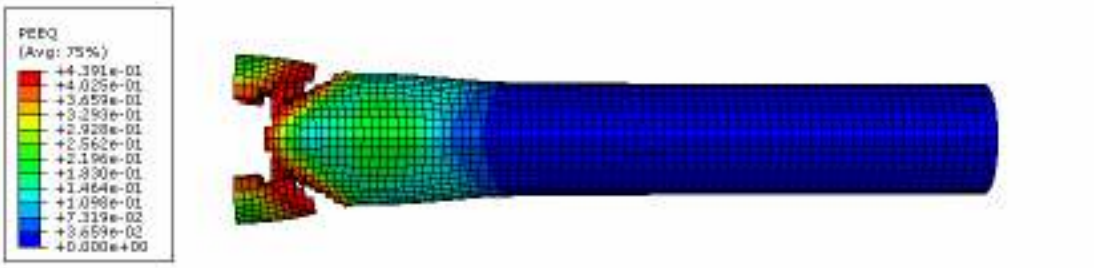

Figure 4.15. After removing elements with equivalent plastic strain higher than 0.44.

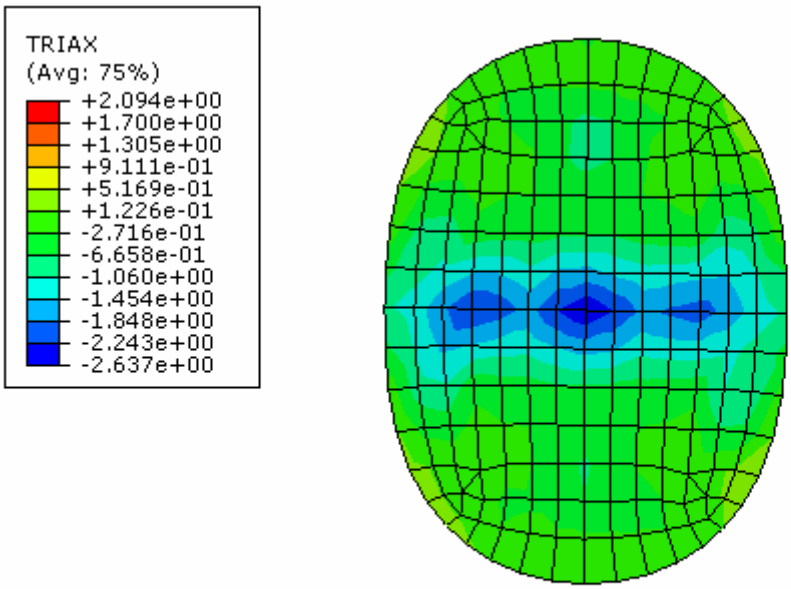

Figure 4.16. The distribution of the stress triaxiality on the impact surface.